UNIVERSITY OF COPENHAGEN

Masters Degree in Physics

Hot Atomic Ensemble for Quantum Enhanced Sensing with Increased Atomic Polarization

Veronika Kaminski

Supervised by Professor Eugene Polzik

August 15, 2023

Veronika Kaminski
Hot Atomic Ensemble for Quantum Enhanced Sensing with Increased Atomic Polarization
Masters Degree in Physics
August 15, 2023
Supervisor: Professor Eugene Polzik

University of Copenhagen
QUANTOP
Masters Degree in Physics
Niels Bohr Institute, Blegdamsvej 17
2100 Copenhagen

Contents

Abstract

Alkaline ensembles in a shielded room-temperature environment have been proven to be a reliable source of atomic ensembles for atom-light interaction as needed for a quantum-enhanced sensing protocol. In the experimental setup presented in this Thesis, Cesium vapor inside an elongated, spin-preserving coated glass channel is optically pumped into a coherent spin state by applying pump and repump light. The atoms are subject to a bias magnetic field introducing Larmor spin precession that is optically read out by a probing beam, transverse to the magnetic field, recorded in a homodyne detection scheme.

Throughout the scope of this Thesis, we used pulsed magneto-optical resonance spectroscopy (pMORS) for atomic spin state characterization and optimization of the experimental setup. We further used this technique to improve the magnetic field homogeneity. We investigated improving the atomic polarization for the atoms in the $F = 4$, $m_F = 4$ ground state level by delaying the turnoff of the pump and repump beams with respect to each other.

Further, we studied the noise reduction of the atomic projection noise through conditional spin state squeezing facilitated by a stroboscopic probing sequence. By reducing the input beam size of the probe light to the acousto-optical modulator, we could reduce the previous minimal duty cycle for the stroboscopic probing sequence. We performed spin squeezing measurements with increased polarization and decreased stroboscopic probe duty cycle to study the influence on the physical system

1

Introduction

The experimental setup presented in this Thesis is used for atom-light interaction with a Cesium ensemble to introduce Faraday interaction in a room-temperature environment.

We utilize the collective spin of the ensemble to interact with probe light. When the ensemble exhibits a non-zero mean spin transverse to the probe light polarization, it introduces a polarization rotation. This effect is referred to as Faraday rotation and can be recorded by a homodyne photo detection scheme [19]. When the probe light travels through an ensemble with zero mean spin, the detection scheme is in balance. With an introduced polarization rotation however, the change of polarization introduces a detectable misbalancing from which we can conclude information about the collective ensemble spin.

Throughout the course of this Thesis, we will utilize the Faraday effect in different ways. Here the experimental setup is centered around a cell containing Cesium vapor that is subject to a bias magnetic field. The atoms are optically pumped into the $F = 4$, $m_F = 4$ ground state by applying an optical pumping scheme. That way we can consider the atomic spin as a collective oscillator, that is oriented by the magnetic bias field.

Firstly, we apply the technique of magneto-optical resonance spectroscopy (MORS). It can be utilized to determine the magnetic field homogeneity, determine the lifetime of a coherent spin state or to classify the atomic polarization.

We use pulsed (p) MORS by applying a fixed RF frequency at the Larmor frequency, which is introduced by the bias magnetic field to determine the quality of the setup. In particular, we characterize the population distribution of the magnetic sub-levels in the ground state and the coherence decay rate for optically pumped atoms.

Further, we will update the optical pumping scheme by introducing a delay between the pump and repump light turnoff. By turning off the repump light earlier, we increase the atomic polarization of the ensemble that can be monitored using pMORS.

Having determined the spin properties, we can move on to classify noise contributions to a probe signal. When reading out the atomic spin, the probe light acts onto the spin state introducing back-action noise. By applying a stroboscopic probing scheme, we are able to reduce that noise contribution. From here we move on and perform conditional measurements to reduce the signal noise in a process called conditional spin squeezing.

By applying pMORS to optimize the experimental setup and stroboscopic conditional measurements to suppress noise, we can use the setup in a quantum-enhanced sensing protocol. The goal of the presented setup will be to detect conductive objects using magneto-induction tomography [13], while exploiting quantum mechanical effects for high-sensitivity detection [27]. In this Thesis, we will focus on preparing the setup so that it will be able to perform the detection of a conductive object afterwards.

Experimental Setup

2

The experimental techniques presented throughout this Thesis are based on atom-light interaction. The following chapter introduces the components comprising the setup as depicted in figure 2.1, alongside a short introduction to the underlying physics. The main emphasis of the theory lies within atomic physics, further reading can be found in [15] on optical physics and in [9] on quantum optics.

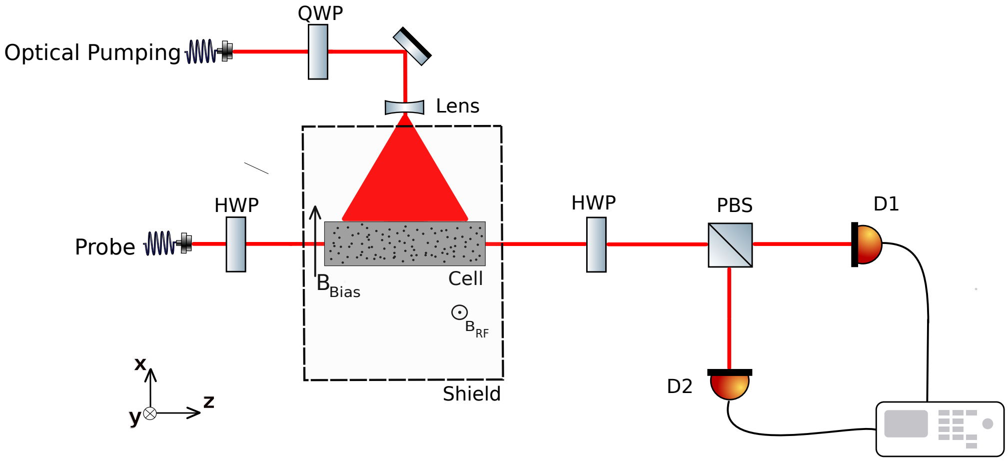

Figure 2.1: Experimental setup as used though out this Thesis

2.1 Atoms and Cell

2.1.1 Atoms

This Thesis covers quantum mechanical atom-light interaction, where the atoms are a macroscopic spin ensemble in the form of an optically pumped Cesium vapor. The following section introduces relevant atomic physics based on the Cesium atom. My main source was [8], follow-up reading can be found in [7]. This Thesis uses the same notation as used at QUANTOP where only upper letters were used to classify the quantum numbers.

Cesium (Cs) is an alkali metal with a total of 55 electrons. Following the 'building-up' principle introduced by Bohr and Rutherford in the 1920s [5], the atomic electrons fill ascending energy levels/ shells and the Pauli exclusion principle limits electrons from falling into lower shells by limiting the number of electrons per shell.

For alkali metals, all electrons are bound to filled shells shells except for of a single unbound valence electron, represented as $6S$ in configuration (2.1) below.

With the *principal quantum number* $N = 1, 2, 3, ...$ counting the shell, the *azimuthal quantum number* $L = S, P, D, ...$ describing the orbital angular momentum of the corresponding shell and the superscripted number showing the numbers of electrons per shell, the electronic ground state configuration for Cesium is

$$1S^2 2S^2 2P^6 3S^2 3P^6 3D^{10} 4S^2 4P^6 4D^{10} 5S^2 5P^6 6S. \tag{2.1}$$

In the ground state, the atomic energy is minimized and every change of the configuration excites the state. Throughout the presented work only transitions between the ground state and the first excited state are relevant and discussed here.

The electrons that are grouped together into completely filled shells (quantized), like $6P^6$, exhibit higher chemical stability than the unpaired valence electron $6S$. As it requires more energy to remove an electron from one of the closed shells than it requires to remove the valence electron, the chemical bonding properties are determined by the free electron [8].

The atomic electrons orbit the nucleus core elliptically at velocities that introduce relativistic effects through spin-orbit interaction, which splits the electron energy levels further into a fine structure, introducing the *orbital angular momentum quantum number* $\mathbf{J} = \mathbf{L} \pm \mathbf{s}$. For a Cs atom, the *spin angular momentum* is $|\mathbf{s}| = 1/2$, where $\mathbf{s}$ remains lower letter to distinguish it from the lowest orbital angular momentum $|\mathbf{L}| = S$.

Focusing on the valence electron for a ground state Cs atom, where $L = 0$, a single fine state with $J = 1/2$ can be observed. In the first excited state $6P$, with $L = 1$, the level is energetically split into two sub-levels for $J = L + s = 3/2$ and $J = L - s = 1/2$. The fine splitting between $6S_{1/2}$ and $6P_{3/2}$ is energetically separated by $\Delta E = 687 \times 10^{-4}$ eV [24], where the level $6P_{3/2}$ has the greater energy.

So far we neglected the nucleus charge. However, the atomic electron creates a magnetic flux $\boldsymbol{B}_e$ that interacts with the nuclear magnetic moment, splitting the electronic energy levels further. Both the valence electron and the nucleus core have a magnetic moment $\boldsymbol{\mu_s} = g_s \mu_B \boldsymbol{s}$ and $\boldsymbol{\mu_I} = g_N \mu_I \boldsymbol{I}$ respectively, where I is the *nuclear spin number*. Here the units of the nuclear magnetic moment and electric magnetic moment, the nuclear magneton $\mu_N = \frac{e\hbar}{2m_p}$ and the Bohr magneton $\mu_B \frac{e\hbar}{2m_e}$ are related by the electron-to-proton mass ratio

$$\mu_N = \mu_B \frac{m_e}{m_p} \approx \frac{\mu_B}{1836}, \tag{2.2}$$

where m_p and m_e are the electron and proton mass. Consequently, the influence of the nuclear magnetic moment is much smaller than the influence of the electron magnetic moment which causes fine splitting.
With $I = 7/2$ for a Cs atom, the fine structure determined by $\mathbf{L}$ and $\mathbf{J}$, the fine splitting is further refined into the hyperfine levels F. The hyperfine interaction is proportional to $\mathbf{J} \cdot \mathbf{B}_e$, causing $\mathbf{I}$ and $\mathbf{J}$ to change direction, while the total angular momentum of the atom $F = I \pm J$ remains constant. The total atomic angular momentum is $F = \{|I - J|, |I - J| + 1, ..., |I + J|\}$, introducing a $m_F = (2F + 1)$-fold degeneracy.
For a $6S$ ground state Cs atom, the total atomic angular momentum causes hyperfine splitting into $F = I + J = 7/2 + 1/2 = 4$ and $F = 3$ manifolds. For the first excited state $6P$, we obtain two hyperfine sub-levels for $6P_{1/2}$ with $F' = 3, 4$ and for $6P_{3/2}$ we see four sub-levels $F' = 2, 3, 4, 5$, where the excited state is denoted with F'.

Fine and hyperfine transitions are determined by dipole allowed transitions. Selection rules for electric dipole transitions include $\Delta L = \pm 1$, $\Delta J = \pm 1, 0$ and $\Delta F = \pm 1, 0$ with the exception of $F = 0 \rightarrow F = 0$ not being included [7]. With our choice of experimental setup, we are interested in the $6S_{1/2}$ ground state and the first excited stated $6P_{1/2}$ and $6P_{3/2}$, all of which can be seen in figure 2.2. A list with possible transitions for both the fine and hyperfine splitting can be found in [24].

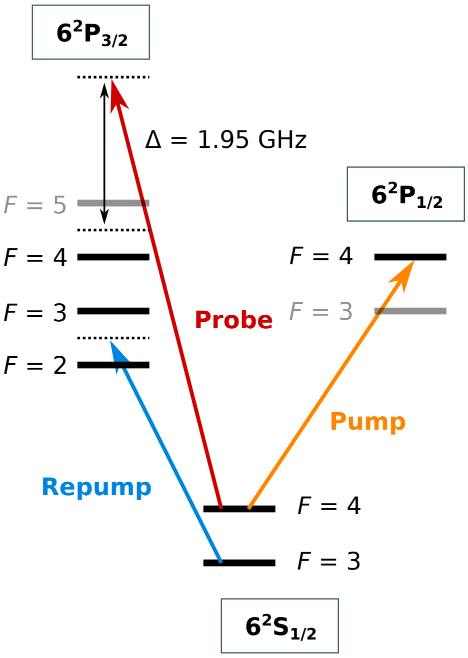

Figure 2.2: Relevant hyperfine levels of the Cesium ground state and first excited state. Figure kindly provided by R. Schmieg [21]

2.1.2 Cell and Shield

In the presented experiment, we use Cesium-133 (^{133}Cs), the only stable Cesium isotope [24]. The atomic spin ensemble is contained in a 500 µm × 500 µm × 25 mm glass channel which is placed inside a chip, mounted inside a sealed glass tube. A glass stem, that contains a Cesium drop evaporating Cs vapor, which leads to a number of atoms N_A distributed evenly through out the channel, is attached to the tube. The cell temperature is set to approximately 55 °C to increase the atomic density in the cell compared to the cell at room temperature. An exemplary vapor cell with chip can be seen in figure 2.3.

To maintain the pumped spin polarization and prolong the atomic coherence, an anti-relaxation paraffin coating is applied to the cell walls. When atoms bump into the coated cell walls, the spin state is preserved and the atomic coherence is maintained for $> 10^4$ wall collisions.

The cell was produced in-house, using glass-blowing techniques by Mikhail V. Balabas. Further information on the cell fabrication process and testing can be found in [21]. A picture of the cell can be seen in figure 2.3.

To obtain information about the atomic spin state, we send a probe beam

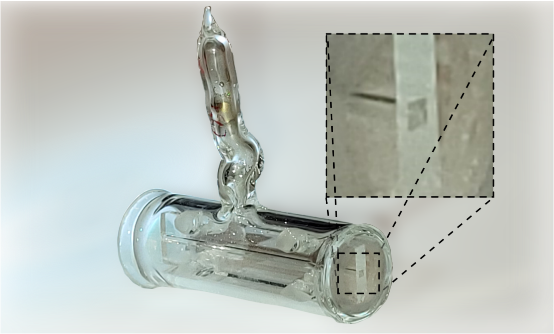

Figure 2.3: Picture of exemplary cell with chip and channel, kindly provided by Ch. Baerentsen [4]

through the elongated channel, where we aim for maximized probe beam transmission. Typically we obtain a transmission of $(88 \pm 1)\%$, where losses are due to the cell coating, reflections, absorption and unwanted clipping losses. We ensure the transmission with both camera recordings of the channel and by use of a power meter.
The production and further cell characteristics are described in detail in [21] and N_A was determined using absorption spectroscopy and yielded $N_A = (1.51 \pm 0.01) \cdot 10^9$ atoms for a temperature of 55 °C.
While working with the cell, we regularly observed performance degradation like an increased signal linewidth as described in chapter 3. To improve the cell performance, the cell can be heated up to 70 °C and is then slowly brought back to room temperature in a process described as recuring in [21].
Throughout the time I spent working on the presented setup, we had to recure the cell with increasing frequency, which usually had an immediate effect on the cell performance. However, that came at the expense of losing one to two days while waiting for the cell and re-inserting it in the experimental setup.

To ensure that no external magnetic fields compromise atomic signals by disturbing the spin state or altering the Larmor frequency, the cell is placed inside a cylindrical magnetic shield. The multilayered shield is constructed of an aluminum layer, followed by three layers of mu-metal enclosed by an iron layer. The shield composition can be seen in figure 2.4. We ensure the absence of unintentional magnetic fields by regular degaussing of the shield. Further details on a similar shield and the process of degaussing can be found here [23].

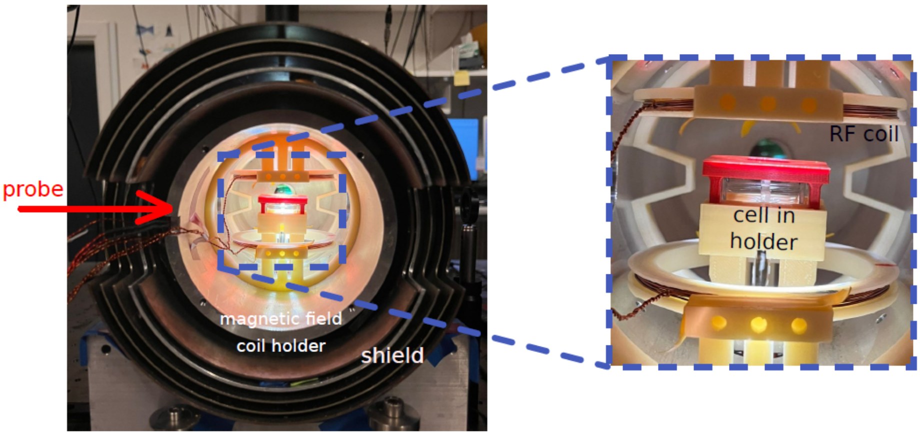

Figure 2.4: Picture of the experimental setup of the cell inside the shield. Shield comprising of five metal layers to buffer external magnetic fields, a holder for the applied bias magnetic field, the RF coils and the Cs vapor cell contained in its holder

2.2 Magnetic Fields

During the experiment we rely on orienting the atomic ensemble spin by applying a magnetic bias field. The following section will first introduce the influence of a static magnetic field on the atomic ensemble, followed by presenting the magnetic field composition used in the experimental setup.
My main source the underlying atomic physics in section 2.2.1 was [8], a more in-depth introduction can be found in [7].

2.2.1 Atoms in Magnetic Fields

Without an applied magnetic field or polarizing laser, the orientation of the magnetic moment of the atomic ensemble is random, and the net magnetization averages to zero. Experimentally that is the case when we place the vapor cell into our shield without any active magnetic fields.
Following [8], we can resort to the classical picture of an oscillator and describe an electron as a three-dimensional harmonic oscillator with resonance frequency ω_0 with the same restoring force in all directions.
When a charged particle — in our case an electron with an arbitrary spin orientation — is now subjected to a magnetic field, it experiences Lorentz force that acts on the particle spin and perturbs the oscillation.
For a magnetic field directed along the x-direction, the Lorentz force will

couple the spin orientation in the yz-plane and orient the spin oscillation around the x-axis. Both spin components in y- and z-direction now exhibit the resonance frequency $\omega_0 \pm \omega_L$, while the spin component along the magnetic field orientation remains unchanged. Here ω_L is the Larmor frequency

$$\omega_L = \frac{eB_{bias}}{2m_e},$$

$$\nu_L = \frac{g_F \mu_F B_{bias}}{\hbar} \tag{2.3}$$

induced by the magnetic field. The ensemble spin precesses around the x-axis, pointing in the direction of the field, at frequency ω_L.

The spin component oscillating parallel to the magnetic field radiates electromagnetic waves with linear polarization and frequency ω_0. They are polarized along the direction of the magnetic field and can not be observed in that direction.

The coupling of the y- and z-spin components however, leads to a circular motion in the yz-plane, indicated by the frequency shift $\pm\omega_L$ of the resonance frequency. The circular motion introduces radiation at $\omega_0 \pm \omega_L$. When observed transversely, the circular motion is sinusoidal, so by probing the spin along the z-direction, we observe the y-component.

The ω_L frequency shift and the resulting energetic splitting was first discovered in 1896 by P. Zeeman and is called the Zeeman effect [6].

In section 2.1.1, Cs atoms were introduced as a nucleus core surrounded by stable, electron-filled shells orbited by an unbound electron. As any moving charge, this valence electron creates a magnetic field, the magnetic moment of the atom.

In the absence of external magnetic fields, the total magnetic moment of the atom is a sum of the nucleus moment ($\propto \mu_N \mathbf{I}$) and the electronic moments ($\propto \mu_B \mathbf{J}$), where $\mu_N \ll \mu_B$ and we neglect the nuclear contribution to the magnetic moment. Each of the fine levels J has a degeneracy degree of $m_J = (2J + 1)$.

When we now place the atom inside a static magnetic field $\boldsymbol{B} = B_{bias}\boldsymbol{e}_x$, the interaction is guided by the Hamiltonian

$$H_{ZE} = -\boldsymbol{\mu} \cdot \boldsymbol{B}_{bias}, \tag{2.4}$$

where $\boldsymbol{\mu}$ is constructed by atomic spin ($\propto \boldsymbol{S}$) and orbital ($\propto \boldsymbol{L}$) contributions. When we derive the expectation values of the interaction Hamiltonian in the vector model, we observe an energy shift of

$$\Delta E_{ZE,fs} = g_J \mu_B B_{bias} \Delta m_J, \tag{2.5}$$

with the Landé factor $g_J = 1$ of the total electron angular momentum.
The magnetic field introduces a frequency shift of $\pm\frac{\mu_B B}{h}$ for $\Delta m_J = \pm 1$.
Now we look at the hyperfine structure for an unbound electron with $m_F = (2F+1)$ in a magnetic field and we include both, the nuclear moment $\mathbf{I}$ and electronic moment $\mathbf{J}$ in the total atomic magnetic moment.
We derive the expectation value of the effective Hamiltonian similar to the calculations for the fine structure above and obtain an energy shift of

$$\Delta E_{ZE,hfs} = g_F \mu_B B_{bias} \Delta m_F, \tag{2.6}$$

with

$$g_F = \frac{F(F+1) + J(J+1) - I(I+1)}{2F(F+1)} g_J \tag{2.7}$$

Equations (2.5) and (2.6) remove the degeneracy of the magnetic sub-levels m_J and m_F. They are equally split into discrete energy levels with individual, slightly different Larmor frequencies.
An exemplary shift of the Zeeman spectrum is the energy shift between the $m_F = 3$ and $m_F = 4$ manifolds in the excited $6P_{3/2}$ state for a Cs atom. With a nuclear moment of $I = 7/2$, we obtain $g_F = 0.2$ resulting in $E_{ZE,hfs} = 0.2\mu_B B_{bias}$.
A detailed derivation of the equations presented above can be found [8].

Summarizing above, an oscillating electron in a magnetic field emits electromagnetic waves, acting as a small dipole. That orients the CSS along the Faraday rotation axis introduced through $\mathbf{B}_{bias}$. We can not detect radiation of the electric dipole along the magnetic bias field, so we need to probe perpendicularly. A magnetic field will further act like a perturbation to the hyperfine structure levels, splitting the degenerated m_F sub-levels into equally spaced terms.

Quadratic Zeeman Splitting

For magnetic fields that introduce a Larmor frequency $\nu_L > 1.0\,\mathrm{MHz}$ in the presented experimental setup, we observe the, so-called *strong Zeeman effect*. That effect leads to an uneven spacing of the Δm_F sub-levels described above, the quadratic splitting. The magnetic hyperfine sub-levels are no longer spaced linearly, but dependent on a quadratic splitting frequency

$$\nu_{QZ} = \frac{2\nu_L^2}{\nu_{hfs}}. \tag{2.8}$$

We will revisit that effect for resolved pMORS in chapter 3, where we intentionally increase the magnetic bias field to exceed the spectral signal linewidth for magnetic sub-levels m_F in the $F = 4$ manifold.

2.2.2 Magnetic Fields in the Experiment

The bias magnetic field in the magnetic setup is a superposition of several magnetic fields. They produced by coils that are mounted on a coil holder that is implemented inside the shield. The coil holder can be seen in figure 2.4. The magnetic coils create a highly homogeneous field throughout the cell dimensions. That way we obtain a static magnetic field, inducing a stable Larmor frequency.

The collective description of the bias field includes a main field B_x, a saddle coil, a compensation coil and smaller B_y and B_z components.
The main field contribution B_x is oriented in the direction of the pumping beam and has the highest influence on the Larmor frequency. It creates a field that orients the atomic spin along the x-direction, leading to a spin precession at the Larmor frequency the x-axis direction.
The saddle coil corrects the radial field gradient and together with the compensation coil, it improves the field homogeneity throughout the cell dimensions.
B_y and B_z contribute to the magnetic field transverse to the spin read-out component and have the least impact on the system performance and the spectral signal, which will be introduced in the next chapter.
All field components can be addressed individually and will be optimized further in the following chapter.

2.3 Lasers

2.3.1 Light as Quantum Mechanical Operator

Whenever we utilize light experimentally, we use it to interact with the atomic ensemble. To prepare the atoms into a collective coherent state with a high polarization, we optically pump the atoms by applying circularly σ_+ polarized light. Subsequently, the atomic spin state is recorded by applying a linearly polarized probe beam in a balanced homodyne detection scheme, which can be seen in figure 2.6 and will be described in section 2.3.3.

The polarization of the applied light is directly associated with the direction of the electric light field [26] and can be described using the Stokes operators [16]

$$\begin{aligned} \hat{S}_x &= \frac{1}{2}(\hat{n}_x - \hat{n}_y), \\ \hat{S}_y &= \frac{1}{2}(\hat{n}_{+45^\circ} - \hat{n}_{-45^\circ}), \\ \hat{S}_z &= \frac{1}{2}(\hat{n}_{\sigma+} - \hat{n}_{\sigma-}). \end{aligned} \tag{2.9}$$

In the presented setup the probe light is highly polarized in x-direction, so we can replace $\hat{S}_x$ with the classical number S_x [11].
Analogous to the classical oscillator, we can further redefine the canonical light operators as $\hat{x}_L = \frac{\hat{S}_y}{\sqrt{S_x}}$ and $\hat{p}_L = \frac{\hat{S}_z}{\sqrt{S_x}}$, which can be expressed in terms of the creation and annihilation operators $\hat{a}$ and $\hat{a}^\dagger$ [9].
The Stokes operators follow

$$[\hat{S}_i, \hat{S}_j] = \epsilon_{ijk} i \hat{S}_k \text{ and } [\hat{x}_L,\ \hat{p}_L] = i \tag{2.10}$$

according to the commutation relations for angular momentum following the definition introduced in [16] and [9].
From the non-commutativity of the operators we obtain the Heisenberg Uncertainty relation

$$\mathrm{Var}(\hat{S}_y) \cdot \mathrm{Var}(\hat{S}_z) \geq \frac{S_x^2}{4}. \tag{2.11}$$

2.3.2 Optical Pumping

Atomic Spin Preparation

From the description of an individual atomic spin of a Cs atom in terms of its quantum numbers in section 2.1.1, we generalize to an atomic oscillator ensemble in this section, where the ensemble size provided by the cell can be considered macroscopic [11].
The atoms are uncorrelated, so we can assume $\hat{\mathbf{J}} = (\hat{J}_x, \hat{J}_y, \hat{J}_z)$ to be the sum of all individual atomic spins $\hat{\mathbf{J}}^i$ [14].
Without external electromagnetic interaction, the atomic spin $\mathbf{J}$ follows a thermal distribution

$$\hat{J}_x^2 = \hat{J}_y^2 = \hat{J}_z^2 = \frac{F(F+1)}{3} \overset{F=4}{=} \frac{20}{3}, \tag{2.12}$$

in the $6^2S_{1/2}$ ground state. The ensemble has a mean spin $\langle \hat{J}_i \rangle = 0$ and the corresponding variance $\mathrm{Var}(\hat{J}_i)_{thermal}$ is called *thermal noise*.

With the $m_F = 2 \cdot F + 1 = 7$ hyperfine Zeeman sub-levels in the $F = 3$ manifold and $m_F = 9$ degenerated hyperfine sub-levels in the $F = 4$ manifold, Cesium atoms can be found in 16 Zeeman ground state levels. In a thermal state, the population of the individual sub-levels is equally distributed with the $F = 4$ manifold signal containing $\frac{9}{16}$ of the atoms. For a thermal state we consequently observe $\mathrm{Var}(\hat{J}_z)_{thermal} = \frac{20}{3} \cdot \frac{9}{16} N_A = \frac{15}{4} N_A$, which will later be referred to as thermal noise in chapter 5.

To reduce the thermal noise, we experimentally redistribute the ground state population of the $F = 3$ and $F = 4$ manifold into the $F = 4$, $m_F = 4$ state, the coherent spin state (CSS). Due to our choice of atomic manipulation through the pumping lasers, which can be seen in figure 2.5, this is a dark state. The state can not be addressed by the pumping lasers for further excitement from the ground state [3].
With an applied magnetic bias field in x-direction, we can assume x to be our quantization axis and the quantum mechanical operator $\hat{J}_x$ can be exchanged with the classical number J_x.
Compared to the thermal spin distribution (2.12), we expect to observe a noise

reduction for the coherent spin state of

$$\mathrm{Var}(\hat{J}_z)_{CSS} = \frac{FN_A}{2} \overset{F=4}{=} 2N_A = \frac{4}{15}N_A = \frac{8}{15}\mathrm{Var}(\hat{J}_z)_{thermal}, \tag{2.13}$$

reduced by a factor $\frac{8}{15}$ compared to the thermal noise of a spin state in the $F = 4$ sub-level. The corresponding variance $\mathrm{Var}(\hat{J}_y)_{CSS}$ is the *projection noise* of the coherent spin state, which is minimal.

The percentage of atoms in the $F = 4, m_F = 4$ ground state is the atomic polarization p and if all ensemble atoms are in the dark state ($p = 1$), the atomic projection noise as seen in equation (2.13), is minimized.

We were able to experimentally verify a polarization of $p > 98.0\%$. The corresponding experimental measuring technique will be introduced in chapter 3.

It should be noted that some sources refer to the thermal noise as projection noise of a thermal state.

Pumping Light

To obtain a highly polarized CSS we optically pump the atoms.

In the experimental setup, we resort to a combination of a pump and repump laser to address atoms in the $F = 3$ and $F = 4$ ground state hyperfine manifolds respectively.

The pump laser is a σ_+-polarized laser with wavelength $\lambda = 894\,\mathrm{nm}$ that is locked to $F = 4 \rightarrow F' = 4$ transition, addressing the Cesium D1 line.

The σ_+-polarized light lifts atoms from any sub-level m_F in the $F = 4$ manifold into $F' = 4, m'_F = m_F + 1$ of the first excited state $6P_{1/2}$, where $m_F = \pm 4$ are the maximally reachable sub-levels. From $F' = 4$ the atoms decay, based on the selection rule $m_F = (m_{F'} - 1, m_{F'}, m_{F'} + 1)$, back into the ground state $F = 4$. From here atoms that are not already in the $m_F = 4$ state, are addressed by the pump laser again to undergo the same process until they finally decay into the dark state, where it can not be addressed further.

However, that process only redistributes atoms in the 4 manifold.

To lift atoms from the 3 manifold into the 4 manifold, we address them with additional light, the repump laser, a σ_+-polarized laser with wavelength $\lambda = 852\,\mathrm{nm}$, locked to the $F' = 2, 3$ cross-over transition on the Cesium D2 line. The repump laser excites atoms in the $F = 3$ ground state manifold into the excited state $6P_{3/2}$, from where they can decay back into the $F = 4$ ground

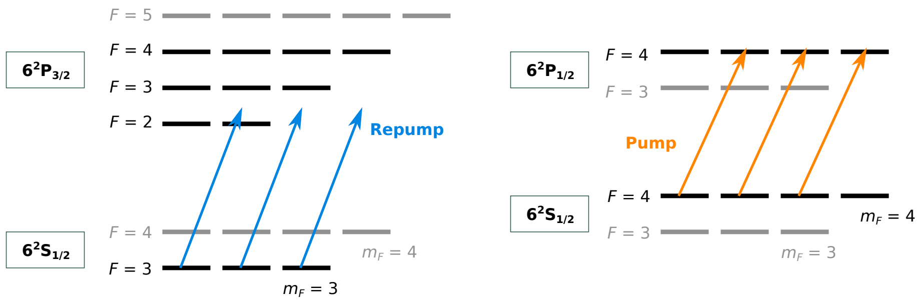

Figure 2.5: Optical pumping scheme, left picture shows the redistribution of the atoms in the $F = 3$ manifold with the goal of moving them to the $F = 4$ manifold in the GS, the right picture shows the pumping of atoms in the $F = 4$ manifold with the goal of moving them into the $m_F = 4$, $F = 4$ dark state. Figure kindly provided by R. Schmieg [21]

.

state manifold, where they can be addressed by the pump light and moved towards $m_F = 4$.

The optical pumping scheme for the pump and repump laser can be seen in figure 2.5.

The lasers are temporally and spatially shaped by an array of electronics and optics, the logic trigger lines can be seen in figure 3.2. Both pump and repump laser are operated with pulsed sequences, prepared by individual acusto-optical modulators (AOMs), where each of the lasers is modulated by the first-order diffraction mode of an individual AOM. Different to the probe sequence introduced in chapter 4, the pump and repump light are turned off smoothly, which can be seen in figure 2.1.

After the individual temporal beam shaping, the pump and repump laser pass through individual half-wave plates that can be used to change the pump and repump laser power before the two beams are overlapped into a single beam by a beamsplitter. Subsequently, the single beam is sent it through a fiber to the experimental setup. In front of the cell, the beam is broadened to address all atoms in the cell homogeneously.

Spin Coherence Time

After we stop the optical pumping, the atoms in the CSS undergo a multitude of decohering effects and the spin distribution exponentially decays towards a thermal ground state. The time $1/\exp(-t)$ of the CSS is maintained after the pumping has been turned off is the coherence or spin relaxation time.

We differentiate between the *longitudinal coherence time* T_1 for spin components oriented along the bias magnetic field, in our case along the x-axis and the

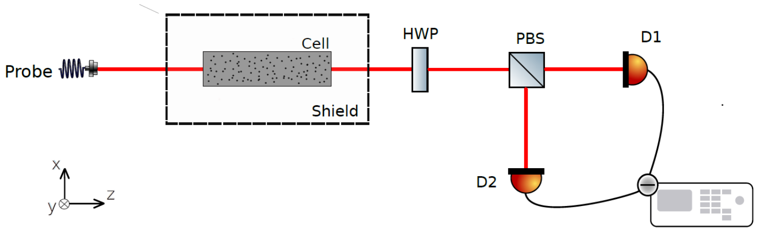

Figure 2.6: Schematic setup of homodyne detection scheme for probing after the cell as used in the experimental setup. Half-wave plate and polarized 50/50 beam splitter used to balance the signal

transverse coherence time T_2.
Throughout the course of this Thesis, we are mainly interested in T_2. The decay of $\hat{J}_\perp$, spin components orthogonal to the bias magnetic field are governed by the evolution of the mean spin

$$\langle \hat{J}_\perp(t) \rangle = \langle \hat{J}_\perp(t=0) \rangle \exp\left(\frac{-t}{T_2}\right), \tag{2.14}$$

dependent on T_2 [21].

2.3.3 Optical Read Out

To read out the evolution of the atomic population distribution, we apply probing light with a wavelength $\lambda = 852\,\mathrm{nm}$, that is linearly polarized in x-direction. The light is 1.95 GHz blue detuned from the $F = 4 \rightarrow F' = 4,5$ cross-transition on the Cesium D2 line to avoid absorption and to probe using Faraday interaction.
The spin polarization can be observed perpendicular to the bias magnetic field and with a magnetic field that orients the spin to oscillate around the x-axis and a probe beam propagating in z-direction, we can observe the y-and z-components $\hat{J}_y$ and $\hat{J}_z$ of the spin precessing motion.

To detect the probe beam, we use a homodyne detection scheme that can be seen in figure 2.6. Upon interacting with the atoms and propagating through the shield, the linearly polarized light is split by a polarized beam splitter and detected through a balanced photodetector (BPD). When the probe light interacts with non-polarized atoms in a thermal spin distribution, the detected signal is equal for both detection paths of the homodyne detection scheme. After interacting with polarized atoms in an oriented CCS, the linear polarization of the probe beam shifts and the BPD detects an intensity change between the detection paths. Detailed information on homodyne detection can be found in [12].

Technique: pulsed MORS

3

The previous chapter introduced atom-light interaction with optically pumped Cs atoms inside a static magnetic field. With the setup presented in chapter 2, we expect a coherent spin state (CSS) with the collective spin precessing around the orientation of the bias magnetic field. To obtain a high polarization of the $F = 4$, $m_F = 4$ ground state as seen in equation (2.13) using optical pumping, in a homogeneous bias magnetic field, we expect to observe spin-induced noise for the spin component transverse to the bias field when we optically read it out.

To experimentally determine the quality of our setup for spin preparation, we use magneto-optical resonance spectroscopy (MORS). This technique allows to improve the optical pumping efficiency, bias field homogeneity and quantify the atomic characteristics of the cell [21]. The following chapter will give a brief overview of the (p)MORS technique and its application in the experimental setup presented in this Thesis.

3.1 Introducing an External RF Field

With the combination of pump and repump light presented in section 2.3.2, we optically pump the atomic ensemble into the $F = 4$, $m_F = 4$ ground state level. A bias magnetic field out removes the degeneracy between the magnetic sub-levels and energetically splits between Δm_F.

Throughout the course of this Thesis and commonly used with QUANTOP, we refer to the percentage of atoms in the ground state $F = 4$, $m_F = 4$ as *atomic polarization* p [14]:

$$p = \frac{1}{F} \sum_{m_F=-F}^{F} m \cdot \hat{\sigma}_{m_F, m_F'} = \frac{\hat{F}_x}{FN} \tag{3.1}$$

Using MORS, we experimentally determine p by detecting the population differences between neighbouring Zeeman levels m_F and $m_F \pm 1$.

The following section will give a brief introduction to the underlying physics used for MORS. An elaborate explanation is presented in [14], which was used as the main source for the following section. For the sake of brevity, the notation as seen in [21] was used.

When a spin ensemble is subject to a magnetic field $\boldsymbol{B}$, the interaction Hamiltonian can be written as

$$\boldsymbol{H}_I = g_F \mu_B \boldsymbol{F} \cdot \boldsymbol{B} + O(B), \tag{3.2}$$

similar to equation (2.4). We observe the hyperfine splitting as 3D vector $\boldsymbol{F} = (F_x, F_y, F_z)$ and add a second-order correction term. We now apply a constant magnetic field along the x-axis and an additional oscillating magnetic RF field $\boldsymbol{B}_{RF} = |B_{RF}| \cos(\omega t + \phi)$ along the y-axis, as pictured in figure 2.1. With these fields, we can rewrite the interaction Hamiltonian in equation 3.2 to

$$\boldsymbol{H}_I = \sum_{m_F=-F}^{F} \hbar \hat{\sigma}_{m_F, m'_F} + \frac{g_f \mu_B}{4 N_A} (F_+ B_{RF} e^{-i\omega t} + F_- B^*_{RF} e^{-i\omega t}). \tag{3.3}$$

The bias field introduces a splitting between the m_F levels which can be seen in the first term. The second term introduces oscillating transitions between $\Delta m_F = \pm 1$ sub-levels, where $F_\pm$ is the raising/lowering operator of the spin along the x-axis.
A detailed derivation of equation (3.3) can be found in [14].
By substituting the density matrix $\hat{\sigma}_{m_F, m'_F}$ into the second term of 3.3 and solving the resulting equations of motion (EOM) $\frac{\partial \hat{\sigma}_{ij}}{\partial t}$ for the density operator components, we analytically obtain the transverse spin coherence time T_2, previously introduced in section 2.3.2.
From solving the EOMs we further find

$$\hat{J}_y,\ \hat{J}_z \propto \sum_{m_F=-F}^{F-1} (\hat{\sigma}_{m_F+1, m'_F+1} - \hat{\sigma}_{m_F, m'_F}), \tag{3.4}$$

where neighbouring sub-levels m_F and $m_F + 1$ form one of $2 \cdot F$ two-level systems. Each of the two-level systems exhibits an individual resonance frequency ω_{m_F, m_F+1} and spectral line width Γ_{m_F, m_F+1} which guides $2 \cdot F$ oscillations between neighboring Zeeman levels.

Therefore, when an atomic ensemble is subject to a constant bias and an oscillating transverse RF magnetic field, the hyperfine components $\hat{J}_y$ and $\hat{J}_z$ transverse to the bias field create $2 \cdot F$ two-level systems that interact with the RF field. The RF field introduces Rabi oscillations between neighboring sub-levels m_F and $m_F + 1$, each represented as a two-level system.

Going back to the experimental setup, we apply a pulsed oscillating RF field to the existing setup and drive the m_F sub-level transitions to perform magneto-optical resonance spectroscopy (MORS). The RF field is included in the schematic sketch in figure 2.1 and the coils driving the RF field can be seen in the inset in figure 2.4.
We can read out the resulting transverse spin component $\hat{J}_\perp$ by applying a probe beam that is linearly polarized in x-direction in a balanced homodyne detection scheme, depicted in figure 2.6. The recorded MORS signal is retrieved as time trace that is Fourier transformed to obtain spectral information. Each of the two-level systems $\hat{J}_y$ and $\hat{J}_z$ in equation 3.4 is reflected by a single peak in the spectrum, weighed with a factor $F(F+1) - m_F(m_F+1)$.
By fitting the spectral Lorentzian-like MORS peaks, as seen in figure 3.3, we are able to read out the population difference of neighboring sub-levels to determine the polarisation p.
From the fitted $F = 4$, $m_F = 4$ peak we further read out in the signal linewidth Γ to obtain the inversely proportional transverse spin coherence time

$$T_2 = \frac{1}{\pi\Gamma}. \tag{3.5}$$

To exceed the peak separation compared to the peak width, we utilize a sufficiently high bias field that introduces the quadratic Zeeman effect as seen in equation 2.8.
Usually, we apply a magnetic bias field that induces $\nu_L \approx 1.42\,\text{MHz}$ to separate the peaks of the Zeeman sub-levels and to resolve the signal.
With that Larmor frequency we account for quadratic Zeeman splitting of

$$\nu_{QZ} = \frac{2\nu_L^2}{\nu_{hfs}} \approx 450\,\text{Hz}. \tag{3.6}$$

Here $\nu_{hfs} = 9.193\,\text{GHz}$ is the hyperfine splitting between the $6S_{1/2}$ $F = 3$ and $F = 4$ state.

3.2 Setup and Sequence

As we have seen so far, we rely on an array of precisely timed and shaped lasers and fields when we execute a pMORS measurement. For applications presented later in this Thesis, e.q. in chapter 5, we will operate with pulsed pumping and probing sequences. Consequently, it is beneficial to already use pulsed (p)MORS as opposed to continuous (cw) MORS. The corresponding signal and trigger lines are differentiated into three main purposes: *optical pumping* for spin state preparation, *(stroboscopic) probing* to read out the atomic signal and *signal processing and recording* for data acquisition. The pulsed MORS sequence can be seen in figure 3.1.

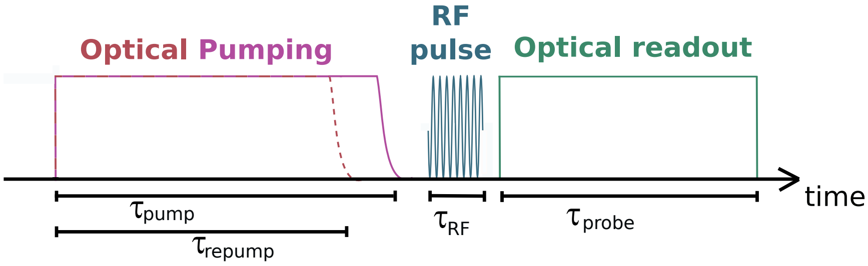

Figure 3.1: Schematic pMORS sequence, where the time between the raising edge of the optical pumping and the falling edge of the optical readout mark the total for one sequence duration T. τ_{repump} is smaller or equal to tau_{pump} with smooth turn off. The RF pulse duration τ_{RF} is followed by optical readout τ_{probe}. Figure inspired by R. Schmieg [21]

The total duration for one MORS sequence is the time between the raising edge of the optical pumping and the falling edge of the optical readout with a total duration $T = 36\,\mathrm{ms}$. The repump time τ_{repump} is smaller or equal to the pump light duration. Non-equal pump and repump light duration will be discussed in section 3.3.

After the optical pumping has been turned off, we introduce a gap to avoid overlapping signals which is typically of the time $\tau_{\mathrm{gap}} = 40\,\mu\mathrm{s}$.

Subsequently, an oscillating magnetic RF field is pulsed for $\tau_{\mathrm{RF}} = 50\,\mu\mathrm{s}$ to drive oscillations of neighbouring m_F sub-levels. That pulse is spectrally broad enough to drive neighboring Zeeman oscillations in the $F = 4$ and $F = 3$ manifolds. That way it is possible to address all ground state Zeeman levels despite their different Larmor frequencies, which have been introduced in section 3.1 [12].

Finally, we send linearly polarized probe light for optically read out of the transverse spin component for up to $\tau_{\text{probe}} = 20\,\text{ms}$.
Both, the pumping and probing duration exceed the transverse spin coherence time T_2 multiple times.

To shape the laser beams spatially and temporally, an array of electronic connections, monitoring and trigger lines is sent by a centralized pulse control, a Quantum Composer (QC). The schematic setup can be seen in figure 3.2.
The QC sequences are set to an internal signal reference T_0 to avoid unnecessary co-dependencies of signal lines throughout the setup and to define and control internal signals.
Both pump and repump pulses are shaped by an individual voltage-controlled oscillator (VCO) and a voltage-controlled attenuators (VCA), which are both controlled by a function generator receiving its signal through the QC [18]. We use a low-pass filter for controlling the voltage of the VCA to shape the temporal turnoff of the pumping pulses. That reduces atomic excitation induced by higher frequency components in the Fourier transformation.
From the VCO and the VCA, the signal is sent to a switch, which triggers a sharp turn on of the pulses.
Subsequently, the signal is sent to an AOM for diffractive pulse shaping, where we use the first-order diffractive mode.
The signal lines are similar for pumping and probing with the difference that the probe beam is turned on and off with a sharp edge, whereas the pumping beams are turned off slowly, so for the probe beam there is no low-pass filter added so that the sequence duration for the probe can be pulsed in chapter 5.
Ina previous publication [27], data traces were recorded using a Spectrum Analyser card. In the process of improving the setup, we updated the means of recording to obtain a larger number of data points in the spectral region of interest, as proposed in [21]. We now use a LeCroy Wavesurfer Oscilloscope to record the data traces for an increased sample number and averages. To analyze the MORS signal, we add a fit to the obtained spectral data points. With an increased number of recorded data points, we were able to obtain an improved performance of the fitting function for increased spectral resolution. We further implemented an additional fitting function to the Fourier-transformed spectrum that utilizes a complex model fit for improved fit performance [21]. The originally used thermal model fit does describe the overall signal behavior, however it does not reflect the actual data to the precision that is needed

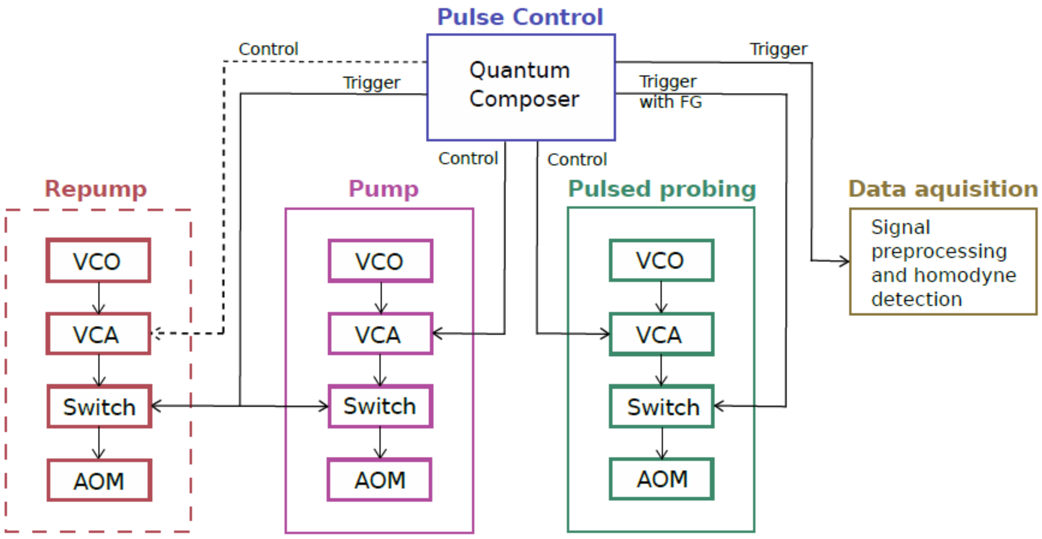

Figure 3.2: Schematic pulse and trigger lines for optical pumping, probing and data acquisition. Figure adapted from R. Schmieg [21], dashed lines show updated setup for individual pump and repump sequence control.

to investigate the exact polarization evolution and overestimates polarization, while underestimating the line width. Further information on both fit models can be found in [21].

With the pMORS sequence and data acquisition set, we can now move on to observe the resulting spectrum and effects that influence the signal.

Let us look at figure 3.3 which visualizes the influence of pump and repump light on the signal. All three spectra were obtained using high-frequency pMORS with an RF frequency $\omega = 1.42\,\mathrm{MHz}$ to individually resolve the spectral peaks. The magnetic fields, as seen in 2.2 are active and optimized for high field homogeneity. Pump and repump light is turned on for 12 ms per sequence and the data traces were recorded with 200 averages for 2 ms/div with an RF amplitude of 400 mVpp.

Figure 3.3(a) shows an atomic ensemble that is prepared only with repump light at an input power of 350 µW. The laser power was measured with a power meter in front of the cell at 300 averages.
In the spectrum, where we expect the $F = 3$ manifold, between 1.415 and 1.422 MHz, there is one small bump is visible, showing that the atoms in the

$F = 3$ manifold have successfully been pumped into the $F = 4$ manifold. $F = 4$ is visible in the comb structure between 1.416 and 1.421 MHz.
Pumping the atoms with σ_+ polarized pump light into the $F = 4$ state is an anisotropic process. While pumping, an atom is moved towards a higher m'_F sub-level than the sub-level it was before pumping, leaving more atoms in higher than lower sub-levels. Peaks for lower frequencies correspond to population differences between higher m_F sub-level and thus we are ultimately interested in the peak furthest to the left, which shows Rabi oscillations between $m_F = 3$ and $m_F = 4$ sub-levels in the $F = 4$ manifold.

In comparison, only pump light was active for figure 3.3(b) with an input light power of 110 µW. Compared to figure 3.3(a), we address atoms in the $F = 4$ manifold and redistribute them towards the $m_F = 4$ sub-level with a Larmor frequency $\nu_L = 1.417\,\text{MHz}$. The $F = 3$ manifold can be seen in the inset in figure 3.3(b) and remains untouched and atoms there are equally distributed between all sub-levels.
We obtain a linewidth $\Gamma = 320\,\text{Hz}$ and polarization $p = 95.3\%$ and observe a peak separation between $F = 3$ and $F = 4$ of $\nu_{\text{quad}} \approx 450\,\text{Hz}$,which corresponds to equation (3.6).

In figure 3.3(c), both pump and repump were active with 110 µW and 350 µW laser power in front of the cell respectively. The signal peak position for $F = 4$, $m_F = 4$ remains unchanged, but almost all atoms in the $F = 3$ manifold are redistributed into $F = 4$.
We see an additional peak indicating the occupation oscillation between the $m_F = 3$ and $m_F = 2$ sub-levels. This peak will be removed in section 3.3 where the population of the peak will be moved into the $m_F = 4$, $m_F = 3$ peak. The linewidth is reduced to $\Gamma = 220\,\text{Hz}$ with a polarization of 96.7 %, which shows the importance of sufficiently optimized optical pumping for both pump and repump.
From figure 3.3 we can further see the importance of a reliable fitting function, as both figure 3.3(a) and 3.3(b) were fitted with a function that is optimized for a spectrum as in figure 3.3(c). Consequently we can assume, that the fit for 3.3(a) and 3.3(b) underestimates the peak height and linewidth and overestimates the polarization. However in figure 3.3(a) we see that the newly implemented complex fit still resembles the data points better than the thermal fit model.

In the process of reviving the setup we also optimized the incident pump and repump beam powers for maximized atomic polarization. The data was recorded as a time traces with 2 msdiv at 200 averages in the high frequency pMORS setting with $\nu_{RF} = 1.42\,\text{MHz}$. The recorded optical pumping power was detected by averaging 300 times with a power meter in front of the cell.
First we scanned the repump power without any active pump light, where we were able to obtain a polarization $p > 80\%$ for repump powers larger than 350 µW, which can be seen in figure 3.4(a). While the polarization in the $m_F = 4$ manifold increases with increasing repump power, the population in the $m_F = 3$ sub-level decreases as more atoms are moved from a thermal distribution towards the $m_F = 4$ sub-level. The population decrease of the $m_F = 3$ sub-level can be seen in figure 3.4(b), where the population is normalized to the thermal distribution.
From the polarization plateau in figure 3.4(a), we can assume 350 µW to be a reasonable input repump power for scanning the pump power.
The polarization does not improve further for pump powers larger than 100 µW as shown in figure 3.5(a). The corresponding occupation reduction for the $m_F = 3$ sub-level can be seen in figure $3.5(b)$.
Both figures 3.4 and 3.5 were only plotted for the more reliable complex model fit, as the thermal model overestimated the atomic polarization, as previously investigated in [21].
Input powers $> 100\,\mu\text{W}$ for pump and $> 350\,\mu\text{W}$ for repump light were found to yield the highest polarization results.

The linewidth is dependent on the magnetic field homogeneity, probe light induced decoherence (see section 5.1) and the performance of the cell coating. Here the field homogeneity was improved by sweeping the current that drives the individual bias field components while taking pMORS traces.
In a combined effort of optimizing the bias field and optical pumping power, recuring the cell and degaussing the shield, we were able to obtain a signal linewidth $\Gamma \approx 150\,\text{Hz}$.

3.3 Improving Polarization with Pump/ Repump Delay

For the previous publication of the experiment [27], pump and repump light were modulated using the same temporal sequence, which was presented in section 3.2. However turning off the repump light prior to turning off the pump light might be beneficial for the ensemble polarization, as observed in [21], promting us to investigate this for this experiment as well.
By turning off the repump light first, while pump light is still active, atoms that are in the $F = 3$ manifold will not be lifted into the $6P_{3/2}$ level, while atoms in the $F = 4$ manifold are still pumped towards $m_F = 4$ sub-level. That could lead to a higher relative probability of $F = 4$ atoms being in the $m_F = 4$ dark state. We trade having atoms in the $F = 4, m_F \neq 4$ sub-levels with more remaining atoms in the $F = 3$ manifold. This however comes at the expense of the total number of atoms in the $F = 4, m_F = 4$ state and we lose optical depth and could reduce the signal-to-noise ratio presented in chapter 5 [21].

To test for improvement of the polarization, we split the control line from the Quantum Composer to the function generator to implement a delay between the turnoff of the pump and repump sequence. We added an additional function generator to the new control line.
A sketch of the setup can be seen in figure 3.2, where the dashed lines represent new added setup line. The switch trigger remains unchanged, as all triggers are referenced to T_0 and we only alter the sequence duration τ_{repump}.

We recorded the data traces with a variation of repump to pump turnoff delay with 345 µW repump and 104 µW pump power at 300 averages the a LeCroy oscilloscope introduced earlier in section 3.2. For comparison, the thermal and complex model fit are included in figure 3.6, where we see that the thermal model fit overestimates the polarization but agrees with the complex fit on the evolution trend of the polarization for increased delay times in accordance with previous observations in [21]. We see a significant increase of polarization from $p = 97.4\,\%$ for zero delay to $p = 98.5\,\%$ for 140 µs delay. A increase in polarization can be seen between 55 and 220 µs delay.

To visualize the loss of optical depth, figure 3.7 shows a reduction of the signal height for increasing pump to repump delay as fewer atoms are lifted from the $F = 3$ to the $F = 4$ manifold. The reduction in signal height is due a loss of optical depth and could negatively influence the signal-to-noise ratio (SNR), which will be discussed in chapter 5.

To summarize the efforts above, we could confirm an increased polarization when the repump light is turned off prior to the pump light using pMORS. For a delay between 55 and 140 µs we were able to increase the polarization by 3.8 ± 1.1 % while reducing the optical depth less than 10 % compared to the optical depth for a simultaneous turnoff.

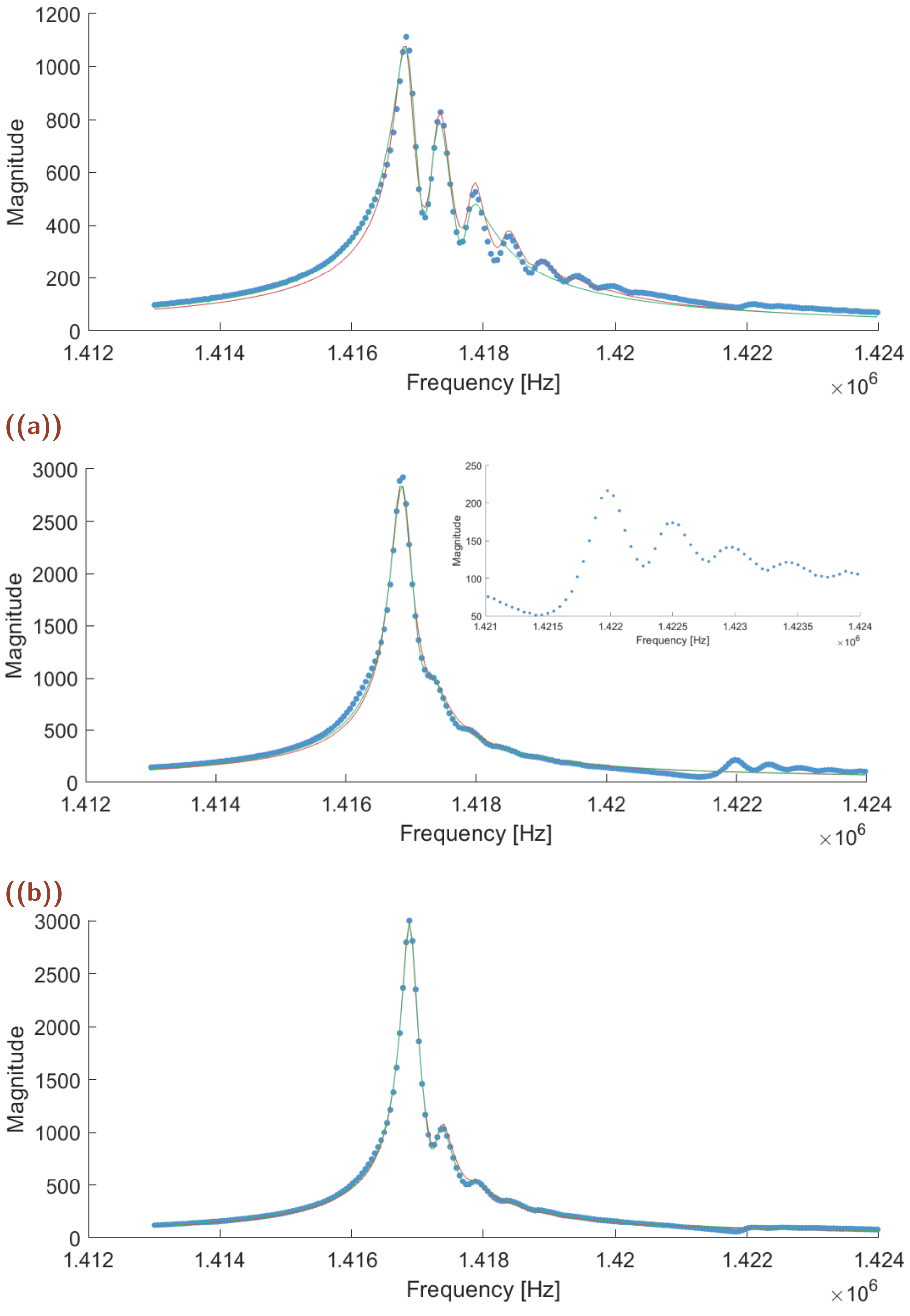

((a))

((b))

((c))

Figure 3.3: Influence of optical pumping on the pMORS spectrum, with complex and thermal model fit for a) only repump light, b) only pump light, c) both pump and repump light active

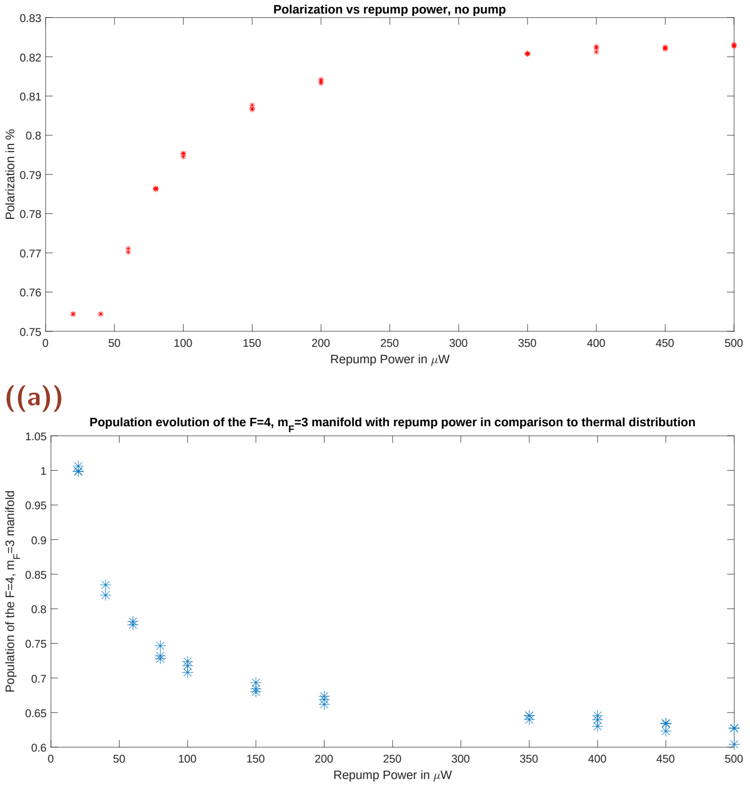

((a))

((b))

Figure 3.4: (a) Evolution of the atomic polarization for the $F = 4$, $m_F = 4$ sub-level with increasing repump power without any active pump light. The polarization reaches a plateau for powers larger than 300 µW, (b) Evolution of the atomic polarization for the $F = 4$, $m_F = 3$ sub-level with increasing repump power without any active pump light, normalized to the initial thermal occupation.

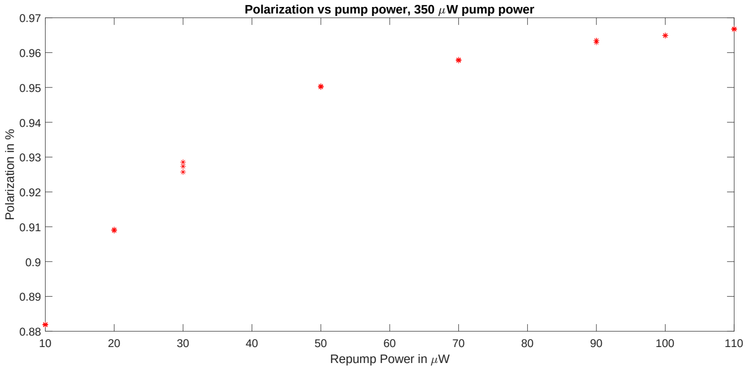

((a))

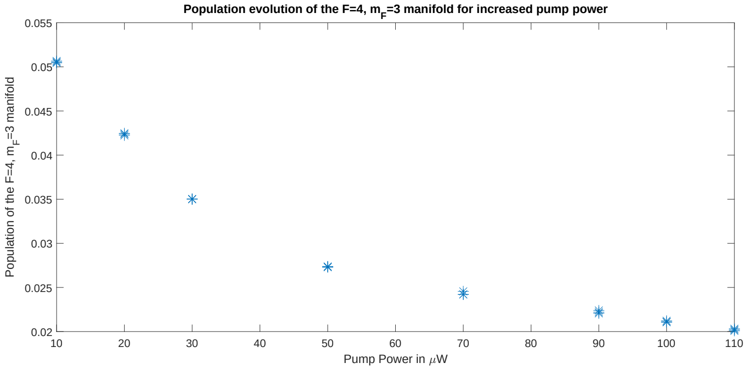

((b))

Figure 3.5: (a) Evolution of the atomic polarization for the $F = 4$, $m_F = 4$ sub-level with increasing pump power and 350 µW (b) Evolution of the atomic polarization for the $F = 4$, $m_F = 3$ sub-level with increasing pump power for 350 µW normalized to the thermal occupation as in 3.4(b).

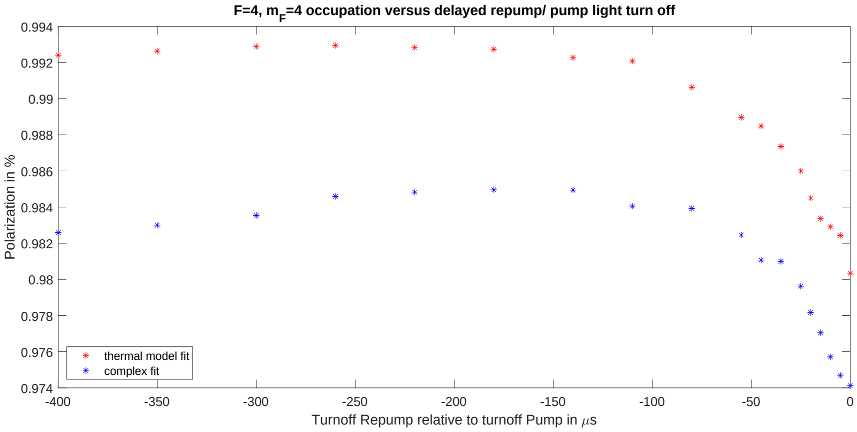

Figure 3.6: Occupation of the $F = 4$, $m_F = 4$ for delayed pump turnoff compared to repump turnoff for complex model fit, which reflects the actual data better compared to the thermal model fit, which shows same trend

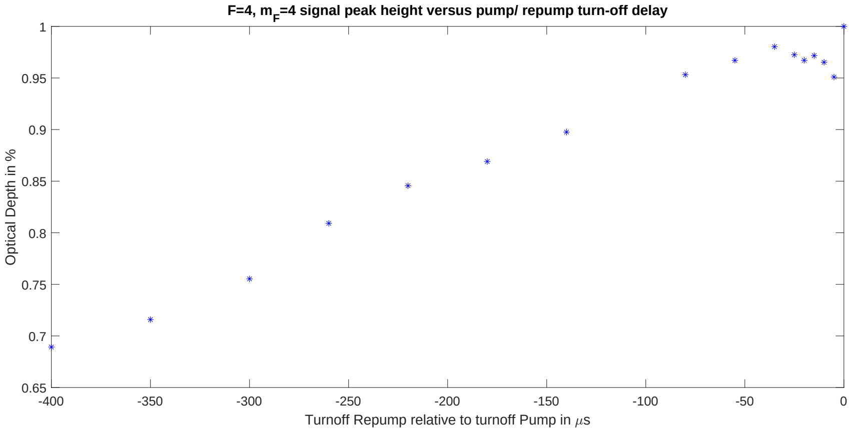

Figure 3.7: Evolution of the $F = 4$, $m_F = 4$ pMORS signal peak height with increasing delay between pump and repump turnoff, normalized to the signal peak height for zero delay to visualize reduction of the optical depth. Same magnetic field and RF settings were used for recording all traces used in this figure

4

Probing Beam Duty Cycle Reduction

4.1 Optical Modulation

In the process of preparing the laser beams for atom-light interaction, we shape the light spatially and temporally. The electronic trigger and signal trail can be seen in figure 3.2.

For temporal shaping, the light it is modulated using an acousto-optical modulator (AOM), where sound waves diffract light into spatially separated diffraction modes. Inside the AOM, the incident light travels though an piezo-electrical transducer with a crystalline structure. By applying an RF signal Λ to the transducer, acoustic waves are formed. The sound waves introduce a periodic compression of the propagation material which changes the refractive index periodically [1]. For sufficiently high acoustic wave powers, the variation of refraction fulfills the Bragg condition

$$m\lambda = 2\Lambda \sin\theta_{bragg} \tag{4.1}$$

for constructive interference and light diffracts similar to atomic lattice diffraction. In equation (4.1), m is the order of diffraction and λ is the incident light wavelength.

A schematic AOM can be seen in figure 4.1

When we assume the experimentally ideal case for constructive interference of plane light and acoustic waves, the Bragg condition is only fulfilled for the first (positive and negative) diffraction order with a deflection angle $\Theta = 2\theta_{bragg}$. Depending on the orientation of the AOM to the beam and hence the Bragg (incidence) angle, light is either scattered in the positive or negative first-order diffraction mode. Light that is not diffracted will remain unmodulated in the zeroth-order.

We intend a high diffraction efficiency, with the majority of light in either one of the first order modes. Experimentally however, we can observe two or

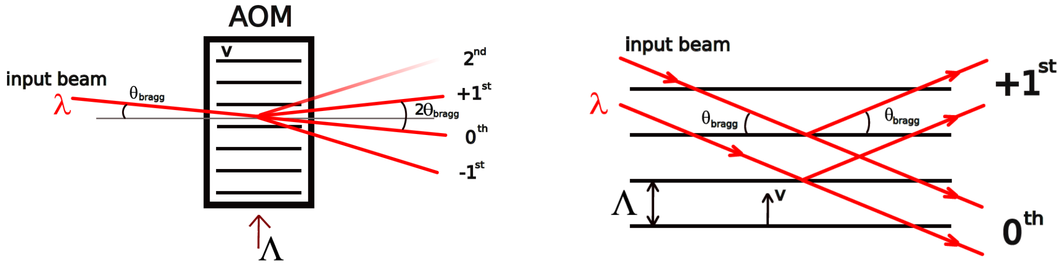

((a)) ((b))

Figure 4.1: a) Schematic setup of AOM. Incident light at wavelength λ is diffracted by acoustic waves with wavelength Λ at velocity v in a piezo-electrical transducer into diffraction mode. b) Bragg diffraction inside an AOM, adapted from [18].

higher diffraction modes which occur due to the finite curvature of the light and acoustic waves.
Consequently to obtain a high AOM efficiency for an incident Gaussian beam, the beam requires a high degree of collimation with a large Rayleigh length to reduce the wavefront curvature.

Overlapping modes can create beating signals in a fiber or on a detector, so we aim for a clear mode separation.
The separation angle between the zeroth and first order modes is twice the incident angle and dependent on the acoustic wave frequency Γ. Hence the beam pointing and mode separation is dependent on the RF frequency and so consequently on the AOM voltage control.

For pulsed probing as described in chapter 5, we operate in a regime with $\nu_{\text{probe}} \approx 1.42\,\text{MHz}$ probing frequency. Different to the pump and repump AOMs that we control such that the beams turne off slowly, we aim for sharp pulses of the probe beam. So besides a high AOM diffraction efficiency, we require a high switching frequency with short rise times for sharp, stroboscopic pulses.
The percentage of time the light is active during one probing sequence is the *duty cycle* D, where the lower limit to the duty cycle is the raise time

$$\tau_R = \beta \frac{d}{v}, \tag{4.2}$$

for beam diameter d and the transducer acoustic velocity v [2]. $\beta = 0.66$ for a Gaussian laser beam and the AOM used in this setup contains a TeO2 crystal with a velocity $v = 4.2\,\mathrm{mm/\mu s}$ [1].

In a previous publication [27], the setup was operated with a probing frequency $\nu_{\text{probe}} \approx 1.42\,\mathrm{MHz}$ at a duty cycle $D = 15\,\%$, which corresponds to approximately $\tau_{\text{probe}} \approx 104\,\mathrm{ns}$ per pulse. Here $D = 15\,\%$ was the lower limit to the duty cycle due to the nature of the experimental setup. However, chapter 5 will introduce that for a pulsed measurement a reduced duty cycle with $D < 15\%$ might be favourable to reduce the quantum noise contribution to the measurement. Further physical introduction can be found in chapter 5, this chapter will focus on the experimental implementation of the duty cycle reduction.

To summarize beam requirements for a AOM setup to successfully reduce the duty cycle duration while maintaining a high efficiency, we need to reduce the beam diameter, while keeping the beam collimated.

So let's look at the light and see how we can achieve a collimated beam with a small beam size. The lasers used in the optical setup emit unmodulated light with a Gaussian intensity distribution. The propagating electrical field has a transverse field measure, the beam width [15]

$$\omega(z) = \omega_0 \sqrt{1 + \left(\frac{z}{z_R}\right)^2}. \tag{4.3}$$

Here ω_0 is the minimal beam waist and $z_R = \frac{\pi \omega_0^2}{\lambda}$ is the Rayleigh length, the distance the beam propagates until it has doubled its cross section, so where $\omega(z_R) = \sqrt{2}\omega_0$. Within the Rayleigh length, the radius of the wavefront curvature is minimized and the better the beam is collimated, the longer z_R [15].

However reducing the beam size of a Gaussian beam while maintaining its collimation requires a slow beam size reduction. Positive lenses with a short focusing length have a small beam waist ω_0 and are effective for a one-step beam reduction. The beam size reduction can be calculated using the ABCD-Matrix formalism [20]

$$\mathbf{r'} = \begin{pmatrix} r' \\ \theta' \end{pmatrix} = \begin{pmatrix} 1 & 0 \\ -1/f & 1 \end{pmatrix} \cdot \begin{pmatrix} r \\ \theta \end{pmatrix} = \mathbf{T} \cdot \mathbf{r}. \tag{4.4}$$

4.2 Updates to Probe Setup

At the distance in the beam path where we set up the AOM, the emitted light has diverged to a beam waist (1050 ± 50) mm.
To obtain a duty cycle $D = 15\%$ with the initial setup, the diverged beam got reduced by inserting a focusing lens with a focal point $f = 250\,\text{mm}$ approximately in that distance in front of the AOM. On the optical table, that corresponds to a beam waist size reduction to approximately $350 - 400\,\mu\text{m}$. For further beam size reduction, we could have exchanged the focusing lens with a lens with higher refraction and shorter focal length. In fact, we could have inserted a lens with e.g. $f = 50\,\text{mm}$ and would have obtained the desired beam reduction. However, that would have increased the beam divergence significantly. Since we are operating with a Gaussian beam, an increased beam divergence decreases the Rayleigh length. With this setup, the Rayleigh length would have been more than one order of magnitude smaller than the AOM length.
Consequently, we aim for a gentle collimating beam reduction by using a telescope setup consisting of two focusing lenses. The first lens has a larger focal length f than the second lens f' and they are separated by the distance $e = f + f'$. The output beam waist is reduced by a factor $\frac{f'}{f}$.

We inserted a total of three telescope setups, which can be seen in table 4.1 and visualized in figure 4.2.

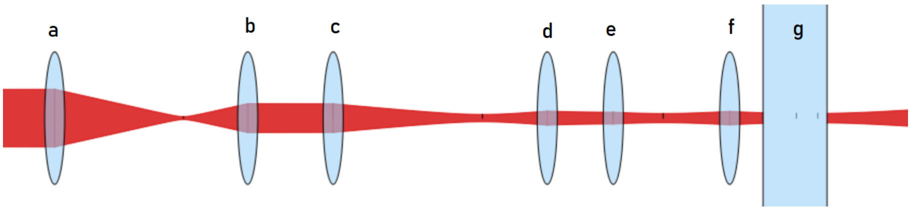

Figure 4.2: Beam size reduction using three telescope setups. a-f: magnifying lenses with $f_a = 200\,\text{mm}$, $f_b = 100\,\text{mm}$, $f_c = 250\,\text{mm}$, $f_d = 100\,\text{mm}$, $f_e = 200\,\text{mm}$, $f_f = 100\,\text{mm}$, g is the AOM inserted such that the middle of the AOM is at the beam waist. The inserted beam waist $\omega_0 = 1000\,\text{mm}$ is reduced to $\omega_0 = 167\,\text{mm}$ with $z_R = 102\,\text{mm}$ at the placement of the AOM. Figure simulated with *Gaussian Beam program* by J. Lodewyck

By using the formalism in equation (4.4), we can calculate the beam reduction

$$\mathbf{r'} = L_{3'} \cdot P_{3'3} \cdot L_3 \cdot P_3 \cdot L_{2'} \cdot P_{2'2} \cdot L_2 \cdot P_2 \cdot L_{1'} \cdot P_{1'1} \cdot P_1 \cdot = T \cdot \mathbf{r}. \qquad (4.5)$$

Lens setup for beam size reduction				
Setup	Focal length f	Focal length f'	Reduction	Experimental z_R
Telescope 1	200 mm	100 mm	0.5	(180 ± 10) mm
Telescope 2	250 mm	100 mm	0.4	(50 ± 5) mm
Telescope 3	200 mm	100 mm	0.5	(27 ± 3) mm

Table 4.1: Table of the lenses used to reduce the beam size, paired in corresponding telescope configurations to demonstrate theoretic beam size reduction per telescope

Here

$$L_i = \begin{pmatrix} 1 & 0 \\ -1/f_i & 1 \end{pmatrix}, P_{i'i} = \begin{pmatrix} 1 & f_i' + f_i \\ 0 & 1 \end{pmatrix}, P_i = \begin{pmatrix} 1 & \omega_i \\ 0 & 1 \end{pmatrix},$$

where L_i is the matrix for beam refraction of a lens with focal length f_i for $i \in \{1, 2, 3\}$, $P_{i'i}$ is the propagation matrix for the distance $f_i' + f_i$ between the two corresponding lenses per telescope and P_i is the propagation distance ω_i between the second lens of a telescope and its beam waist [20]. For a perfectly collimated beam without any beam divergence, the beam size is reduced by the factor

$$T_{22} = \frac{f_{3'}}{f_3} \cdot \frac{f_{2'}}{f_2} \cdot \frac{f_{1'}}{f_1} = 0.1. \tag{4.6}$$

We start out with a beam size (1050 ± 50) µm. The beam geometry is slightly

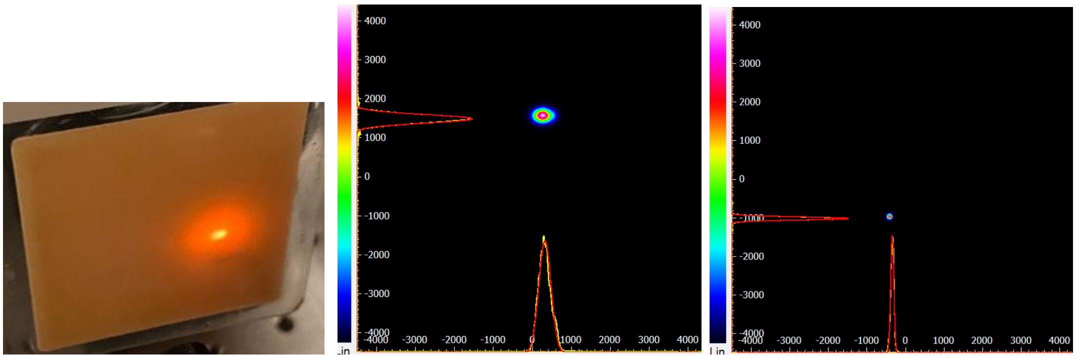

((a)) ((b)) ((c))

Figure 4.3: a) Picture of initial probe beam at the first lens of the first telescope, beam size $\omega \approx (1050 \pm 50)$ mm b) Picture of probe beam at the beam waist behind the second lens of the third telescope c) Picture of probe beam at beam waist behind second lens of third telescope, beam size $\omega = (166 \pm 5)$ mm

elliptic and the beam size has a beam divergence (0.75 ± 0.25) rad. The beam size was recorded using a *ThorLabs Beam Profiler*.
On the experimental table the beam does not look or behave just as depicted in figure 4.2. We have to account for the ellipsoidal shape of the beam and dispersive effects that accumulate when lenses are not hit centrally.
In front of the first lens in the presented setup, the beam has a divergence angle and beam waist position that could only be estimated, which impeded the collimation of the beam so that we end up with a shorter Rayleigh length than simulated.

An example of how the beam looked in the beam path just before the first telescope lens can be seen in picture 4.3(a), the elliptic behavior can be seen in picture 4.3(b) and the final reduced beam at the AOM behind the second lens of the third telescope can be seen in 4.3(c). Here the beam size is (166 ± 5) µm, which corresponds to a beam size reduction of (85 ± 1)%. We were able to maintain a Rayleigh length $z_R = (27 \pm 3)$ mm, which is two times larger than the AOM crystal. The uncertainty is propagated due to the initial elliptic beam.

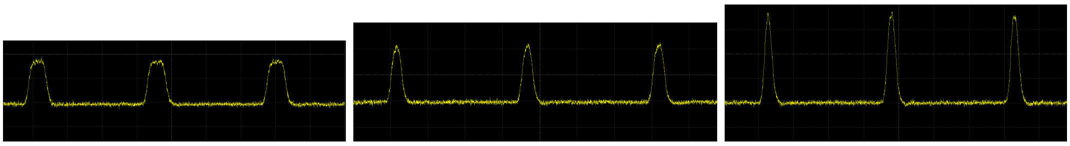
((a)) ((b)) ((c))

Figure 4.4: Time trace of a LeCroy Oscilloscope for a read-out light duty cycle a) $D = 15\,\%$, b) $D = 7.5\,\%$, b) $D = 6\,\%$ for a probing frequency $\nu = 1.450$ MHz, the probe power was not adjusted to visualize the increase of probing photons for a reduced duty cycle, 50 mV/div on the y-axis and 200 ns/div

With the reduced beam size and a new alignment of the AOM, we are able to reduce the probe beam duty cycle from the previous minimum of $D = 15\%$ to $D = 6\%$. In the following chapters we will continue measurements with a lower limit for the duty cycle of $D = 7.5\,\%$. The three duty cycles can be seen in figure 4.4. Here the time traces were taken for a probing frequency of $\nu = 1.450$ MHz and the probe power was not adjusted to visualize how a change of the duty cycle influences the number of photons interacting per time interval.

Technique: Spin State Squeezing

5

In the previous chapters we set the ground for Cesium-based atom-light interaction. Chapter 2 introduced the theoretical descriptions for both, atoms and light, and chapter 3 showed how we can use atom-light interaction employing pMORS to determine the quality of the setup. In this chapter, we will describe the noise contributions to the recorded atomic signals. Knowing these contributions, we will further introduce how to suppress noise using conditional spin state squeezing by applying a stroboscopic probing scheme.

5.1 Noise Contributions

When we optically read out the collective spin state of an atomic ensemble, we use the Stokes operator $\hat{\mathbf{S}}$ to count the number of photons during a fixed unit of time to describe the atomic spin $\hat{\mathbf{J}}$. With the setup pictured in figure 2.1, we use Faraday interaction to optically probe spin component $\hat{J}_z$. As described in section 2.2.1, the probe light is polarized in x-direction and propagating along the z-direction and the bias magnetic field is applied transversely in y-direction.

With that setup in figure 2.1, we detect the y-component of the probe light field, so we are referring to $\hat{S}_y(t)$ as the signal, where the corresponding signal evolution will be discussed in the following section. We record the signal $\hat{S}_y$ after the probe beam has interacted with the ensemble through Faraday interaction to imprint information about the atomic ensemble spin onto the probe light field.

Experimentally, spin and light variables are not only evolving in time due to the desired atom-light interaction but are also influenced by noise contributions that compromise the 'pure' atomic signal. When we talk about signal noise in the following, we are referring to the variation $\mathrm{Var}(\hat{S}_y) = \langle \hat{S}_y^2 \rangle - \langle \hat{S}_y \rangle^2$ of the recorded signal.

The following list classifies photon shot noise, electronic noise, projection noise and quantum noise contributions that influence $\mathrm{Var}(\hat{S}_y)$ throughout the work on this Thesis. The main source for this section was [21], where a more extensive description can be found.

(Photon) Shot Noise

Shot noise quantifies the influence of the probe light on the measurement outcome. With increasing laser power, a larger number of photons arrives at the photodetector and thus the noise contribution increases with the number of probing photons.
The shot noise

$$\mathrm{Var}(\hat{S}_y^{SN}) = \eta(D)\frac{N_{Ph}}{4} \equiv \mathrm{SN}_0, \tag{5.1}$$

scales linearly with the number of photons. Here, D is the probe light duty cycle, which is the percentage of time the probe light is stroboscopically turned on during the period $T = \pi/\omega_L$ and $\eta(D) = 1 + \mathrm{sinc}(\pi D)$. Both the stroboscopic probing and the duty cycle will be introduced further in section 5.2.
From equation (5.1) we see that shot noise does not have a specific frequency and hence is white noise. It remains constant in time for a constant duty cycle and light power.

To record the shot noise signal (SN), we detune the magnetic field so that the resulting Larmor frequency and the corresponding atomic signal are not part of the recorded region of the spectrum anymore. That way we move the atomic resonance signal away and do not drive an atomic signal in the recorded spectral range and are left with the spectrally flat photon noise that we record.
The linear dependency of the shot noise to the probe power can be seen in figure 5.1. The data was recorded with a Spectrum Analyser Card with 500

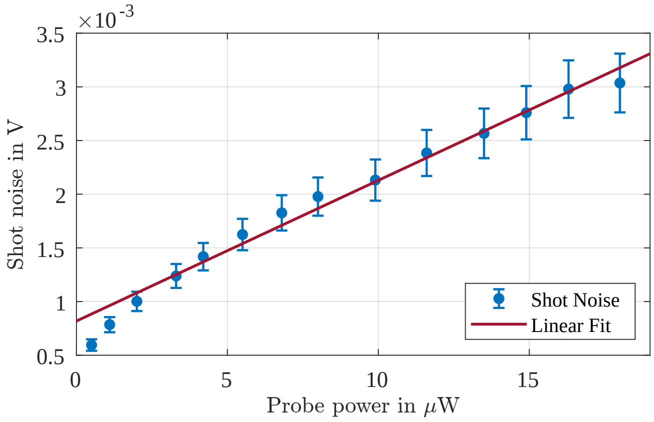

Figure 5.1: Shot noise over probe power with linear fit $f = ax + b$, where $a = 1.31 \cdot 10^{-4}$ and $b = 8.19 \cdot 10^{-4}$, first two data points not included in fit, recorded with Spectrum Analyser Card and 500 Averages

averages.

Experimentally, we have to find a balance between a laser power where sufficient photons interact with the atoms but that does not introduce further decoherence to the CSS. Additionally, the probe power has to be adjusted when we vary the probe light duty cycle so that on average the same number of photons interact.
Though out the measurements presented in this chapter, the average probe power was set to 5 μW. To ensure the accuracy of the incoming photons, we detect the optical power for each measurement with sufficient measurement time.

Electronic Noise

Electronic noise originates from technical components in the setup, e.g. from devices for signal modulation or data recording.
Electronic noise (EN) is an accumulation of possibly noisy components. Consequently, we record EN signals with the same sequence as the atomic signal while both, probe and pumping beams are blocked.
Similar to the shot noise, the electronic noise is a constant background noise to the recording, so we correct the SN in equation (5.1) to the actual shot noise as

$$\mathrm{SN} \equiv \mathrm{SN}_0 - \mathrm{EN} = \mathrm{SN}_0 - \mathrm{Var}(\hat{S}^{\text{no light}})_y. \tag{5.2}$$

Since the shot noise in equation (5.1) can be considered a constant offset to the noise, we commonly use it to normalize the atomic signal and present data in shot noise units (SNU). That way we can compare signals independent of the probe power and electronic noise.

Thermal and Projection Noise

In section 2.3.2 we established optical pumping of the atoms and distinguished unpumped atoms in a thermal state from highly polarized atoms in a coherent spin state (CSS).
In a thermal state, the ground state sub-level population is random so that the mean value of the spin components is zero and all m_F sub-levels are equally populated.
We record the spin noise of a thermal state, the thermal noise (TN) signal with

the same sequence and magnetic fields as the corresponding atomic signal, while blocking the pumping light. With the obtained noise signal we can calculate

$$\mathrm{TN} \equiv \mathrm{Var}(\hat{S}_y^{\mathrm{thermal}}) - \mathrm{EN}. \tag{5.3}$$

From equation (2.13) we know that the thermal noise is increased by a factor of $\frac{15}{8}$ compared to the spin projection noise (PN) of a coherent spin state. Consequently, we can weigh the observed thermal noise to obtain the projection noise

$$PN \equiv \frac{8}{15} TN \tag{5.4}$$

based on the thermal noise measurement.

The evolution of the thermal and projection noise contribution over time can be seen in figure 5.2. Different from the electronic and shot noise, the projection noise is evolving over time due to the influence of the probe light while probing the atoms.

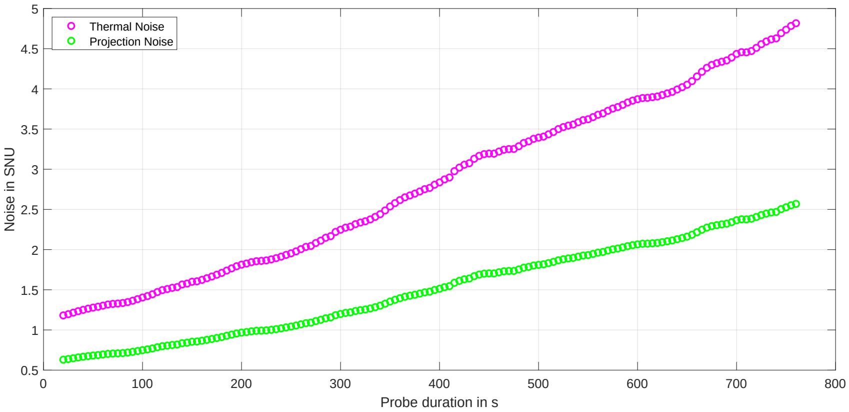

Figure 5.2: Thermal noise and projection noise with increasing probing time, projection noise scales with a factor 8/15 compared to the thermal noise, trace recorded with a probe duty cycle $D = 15\,\%$ and no delay between pump and repump turn off

It should be noted that what is called thermal and projection noise here are additional noise factors imprinted onto the light by the atomic spin. The recorded noise is not the actual thermal and projection noise but rather their effect on the read-out light. The noise described above can be differentiated into classical contributions, like shot and electronic noise and a quantum noise contribution through the projection noise that is increasing due to probing the spin. In the following, we will introduce the measurement-induced quantum mechanical noise

As we established in section 2.3.1, we can assume S_x and J_x to be classical numbers rather than quantum mechanical operators due to the polarization of the probe light and the orientation of the macroscopic spin. We can describe $\hat{J}_y$ and $\hat{J}_z$ as collective spin operators, that are continuous throughout the whole interaction volume of the cell. Consequently, we lose the spacial spin dependency and distinguish the light field $\hat{\mathbf{S}}$ before and after the atom-light interaction.

We can describe the evolution of the input and output light field and the evolution of the atomic spin $\hat{\mathbf{J}}$ with the *input-output relations*:

$$\hat{S}_y^{\text{out}}(t) = \hat{S}_y^{\text{in}}(t) + aS_x\hat{J}_z(t) \tag{5.5a}$$

$$\hat{S}_z^{\text{out}}(t) = \hat{S}_z^{\text{in}}(t) \tag{5.5b}$$

$$\frac{\partial}{\partial t}\hat{J}_y(t) = aJ_x\hat{S}_z^{\text{in}}(t) \tag{5.5c}$$

$$\frac{\partial}{\partial t}\hat{J}_z(t) = 0 \tag{5.5d}$$

where a is constant, which is dependent on the light detuning and frequency. The following notation was adapted from [21], where an extensive derivation of equation (5.5) can be found.

In equation (5.5b) we see the temporal evolution of the Stokes operator describing the light field in z-direction which is only dependent on the input light field of the same direction. The orientation of the presented setup hence makes $\hat{S}_z$ an unsuitable candidate to read out the atomic spin state.

Equation (5.5d) is time and space independent and as such not impacted by the measurement either.

For (5.5c) however, we see how upon interacting with J_x, the input light field $\hat{S}_z^{\text{in}}$ changes the spin components $\hat{J}_y$ over time. This measurement-induced change of the spin component is called *back-action* and is classified as quantum mechanical noise.

Similarly, we see in equation (5.5a) that the output field in x-direction is the sum of the input light field and the interaction of the classical field S_x with the time independent spin component $\hat{J}_z$.

Moving forward we refer to $\hat{S}_y^{\text{out}}(t)$ as the atomic signal.

For a sufficiently large interaction strength, we can use equation (5.5a) as a starting point for a quantum non-demolishing (QND) measurement. By probing in a QND scheme, we are able to reduce the spin-induced noise by decreasing the influence of the measurement on the free evolution of the spin. In section 5.2 we will establish how we can exploit the system dynamics to perform such a back-action reduced measurement.

We can describe the measurement of the output light field in y-direction $\hat{S}_y^{\text{out}}(t)$ by including the dynamics of the magnetic field $H_B = \hbar\omega_L J_x$ to rewrite equation (5.5a) as

$$\hat{S}_y^{\text{out}}(t) = \hat{S}_y^{in}(t) + aS_x \left(\hat{J}_y'(t) \sin(\omega_L t) + \hat{J}_z'(t) \cos(\omega_L t) \right). \qquad (5.6)$$

Here $\hat{J}_y'(t)$ and $\hat{J}_z'(t)$ are slowly rotating spin operators with a sine and cosine component introduced by the additional Hamiltonian [21].
$\hat{J}_y'(t)$ and $\hat{J}_z'(t)$ introduce a time-dependent collective spin precession around the x-axis. Per convention, the atomic sine contribution oscillates in-phase with the input light field in y-direction and the cosine has an out-of-phase contribution. Experimentally we can record both the sine and the cosine component of the light field, however as we will see in section 5.2, we usually only record the cosine component of the light field. Moving forward we will therefore neglect the sine component.

We can use equation (5.6) and rephrase the y-component of the probe light field as a light field that has zero input mean field $\langle \hat{S}_y^{\text{in}} \rangle = 0$ and a non-zero output mean field $\langle \hat{S}_y^{\text{out}} \rangle \approx aS_x \langle \hat{J}_z'(t) \rangle \cos\omega_L t \propto \kappa\sqrt{N_{ph}} \neq 0$. Here we introduced the coupling constant $\kappa = a\sqrt{J_x S_x T}$ of probe light coupling to the spin for a measurement duration T. Additionally, κ characterizes the interaction strength defined by a QND type measurement [25].

We can use κ to rewrite equation (5.6). The full derivation can be found in chapter 3 in [21] and leads to the cosine noise contribution

$$\text{Var}(\hat{S}_y^c) = \frac{N_{ph}}{4} \left(1 + \frac{\kappa^2}{2} + \frac{\kappa^4}{12} \right). \qquad (5.7)$$

Here $\text{Var}(\hat{S}_y^{\text{in}}) = N_{ph}/4$ and since we operate with a coherent atomic state, we can use $\text{Var}(\hat{J}_z) = J_x/2$ [22].

From the signal noise $\mathrm{Var}(\hat{S}_y^c)$ we can now determine the signal-to-noise ratio (SNR)

$$\mathrm{SNR} \propto \frac{\kappa}{\sqrt{(1 + \frac{\kappa^2}{2} + \frac{\kappa^4}{12})}}. \tag{5.8}$$

The larger the SNR, the better the ratio between the desired signal and the perturbing noise. For $\kappa^4 = 12$ we can maximize the SNR and obtain the *standard quantum limit* SQL. The SNR and its maximum can be seen qualitatively in figure 5.9.

Going back to the beginning of this chapter to the list describing the noise earlier in this section, we can relate the recorded noise with equation (5.7). The first term describes the photon shot noise SN. The second term is the introduced projection noise PN, which is growing in time due to the coupling to light. We see that the third term ($\propto \kappa^4 \propto T^2$), the back-action noise, is growing comparatively faster in time than the first two terms. Consequently, we are limited by quantum noise with a contribution that is not only increasing with interaction time, but that is also increasing faster than the shot and projection noise.

5.2 Back-Action Free Measurement

In the previous section we have seen that by optically probing the atomic spin component $\hat{J}_z$, we increase the measurement-induced back-action noise with increasing probing time.

We can counteract that by setting up a measurement where the probe light field does not act on the spin operator $\hat{J}_z$ through the measurement. That way we can record atomic signals with sufficiently large interaction time by exploiting the magnetic bias field-induced dynamic. We refer to such a measurement as a quantum non-demolishing (QND) type measurement, where the measured operator is not disturbed by the measuring operator.

In the experiment presented in this Thesis, we are able to reduce back-action noise by employing a stroboscopic QND measurement. We apply a linearly polarized probe light, that is pulsed at twice the Larmor frequency. That way we can theoretically probe the spin component $\hat{J}_z$ without changing its value during the measurement to maintain a free evolution of the ensemble spin. The following introduction of a stroboscopic QND measurement follows the explanation of [21]. Further reading can be found in [25] and [10].

So far we have only discussed experimental consequences of the quantum back-action noise in the previous section. To understand why we utilize stroboscopic probing, we now take a step back and look at the underlying physics.
From a quantum mechanical point of view, we expect measurement precision limitations for an operator $\hat{X}$, when the operator does not commute with the measurement Hamiltonian $[\hat{H}_I, \hat{X}] = \hat{Y}$. Then the operator obeys the Heisenberg uncertainty principle $\sqrt{\mathrm{Var}(\hat{H}_I)\mathrm{Var}(\hat{X})} \geq \frac{1}{2}|\langle\hat{Y}\rangle|$ [9].
Consequently, the minimal uncertainty, or signal noise for that matter, with which we can measure $\hat{X}$ lies within the uncertainty range $\frac{1}{2}|\langle\hat{Y}\rangle|$.
On the other hand, if an operator $\hat{Z}$ commutes with the Hamiltonian $[\hat{H}_I, \hat{Z}] = 0$, the operator can be measured with arbitrary precision and is not limited by the Heisenberg uncertainty principle. Obviously, this is a theoretical derivation that does not consider 'real world' laboratory conditions that introduce uncertainties like electronic or shot noise.
So to arrange a back-action free measurement of the spin operator $\hat{J}_z$, we aim for conditions that obey $[\hat{H}_I, \hat{J}_z] = 0$ [10].

For the relating orientations as shown in 2.1, [14] showed that with sufficiently far detuned light, the atom-light interaction for probing the setup is guided by $H_I \propto \hat{S}_z(z,t)\hat{J}_z(z,t)$. We can lose the spacial dependency as shown in section 5.1 and rewrite the interaction Hamiltonian in the presence of a magnetic field to

$$H_I \propto \hat{S}_z\hat{J}_z = \hat{S}_z\left(\hat{J}'_z \cos\left(\omega_L t\right) + \hat{J}'_y \sin\left(\omega_L t\right)\right). \tag{5.9}$$

While H_I does not generally commute for $\hat{J}_z$ for $\omega_L \neq 0$, it commutes when $\sin\left(\omega_L t\right) = 0$. Consequently, the commutation relation is fulfilled for $t \equiv n\frac{\pi}{\omega_L}$ for $n \in \mathbb{N}$, or in other words, the condition is fulfilled twice per Larmor precession.
So while we are not able to measure continuously, we are able to exploit the spin precession with Larmor frequency ω_L and measure only when the commutation relation $[H_I, \hat{J}'_z] = 0$ holds. Then the back-action is imprinted onto the $\hat{J}'_y$ component.

This condition can be experimentally realized by strategically modulating the

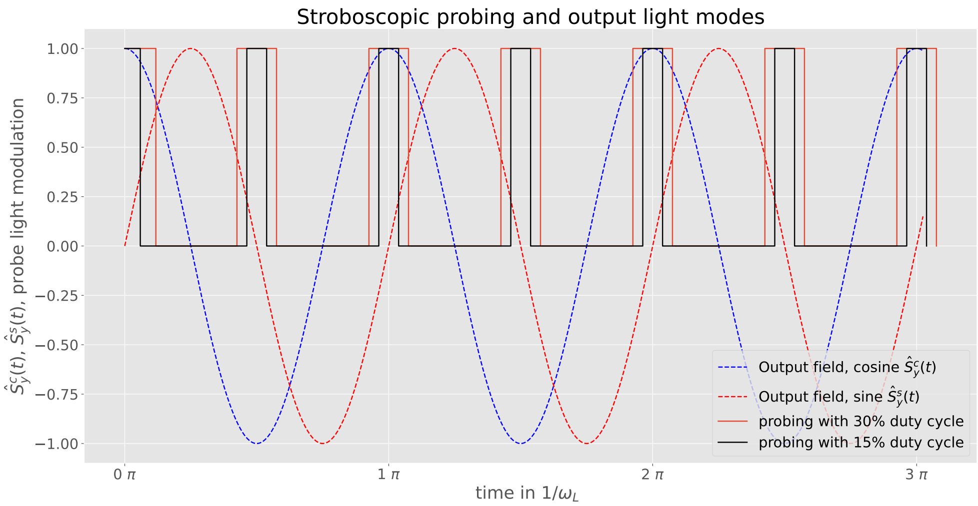

Figure 5.3: Schematic setup of probe modulation to demonstrate increased overlap with the sin component for increased duty cycle

probe light such that we only pulse when $\sin(\omega_L t) = 0$ in equation (5.9). The modulation introduces pulsed probing with a probe pulse rate of $2 \cdot \omega_L$ with a period $T = \frac{2\pi}{\omega_L}$. The width of the arriving pulses is determined by the duty cycle D which was experimentally prepared in chapter 4.

The optical pumping and probing sequences are sketched in figure 5.4. Similar to chapter 3 we optically pump the atoms first, where we can induce an optional delay between the pump and repump light turn off. By turning off the repump light earlier, we achieve a higher atomic polarization of the $F = 4$ manifold, which could help to improve the signal strength. We will investigate the influence of the pump delay in section 5.5. After the pumping has been turned off, we start to optically probe the light with a probing frequency $\nu_{\text{probe}} = 2\nu_L$.

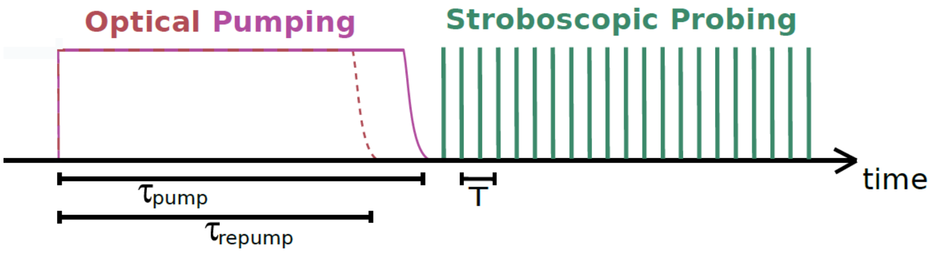

Figure 5.4: Sketched sequence for stroboscopic probing, after the optical pumping has been turned off, stroboscopic optical pulses at twice the Larmor frequency probe with $T = 2\pi/\omega_L$

We are interested in the cosine component $\hat{J}'_z$ and we only want to measure only when it commutes with the interaction Hamiltonian in equation (5.9). Theoretically, that requires an infinitely narrow delta-peak-like probing pulse to fully obey the commutation relation. In the experimental reality, the probe pulse will always have a finite width determined by duty cycle D. Here the duty cycle D is the percentage of time the probe light is active per probing cycle [21].

Consequently, the back-action contribution is dependent on the probing pulse duty cycle.

We can rewrite equation (5.7) for our stroboscopic back-action suppressing measurement to

$$\mathrm{Var}(\hat{S}^c_y) = \eta(D)\frac{N_{ph}}{4}\left(1+\frac{\tilde{\kappa}^2}{2}+C\frac{\tilde{\kappa}^4}{12}\right), \tag{5.10}$$

with

$$\eta(D) = 1+\mathrm{sinc}(\pi D), \quad C = \frac{1-\mathrm{sinc}(\pi D)}{1+\mathrm{sinc}(\pi D)}, \quad \tilde{\kappa} = \sqrt{\eta}\kappa. \tag{5.11}$$

The pre-factor η accounts for the reduced interaction, that comes with duty cycles lower than 1. The factor C quantifies the coupling of the probe noise to the observed spin and can be understood as a qualitative factor to how well the back-action can be suppressed by the measurement scheme [25].

For a continuous measurement, or in other words when $D = 1$, the back action contribution is maximised and equation (5.10) is at its upper limit represented with equation (5.7). On the other end, for a duty cycle approaching zero $(D \longrightarrow 0)$, C approaches the limit $(C \longrightarrow 0)$ and the back-action noise contribution reduces to zero in equation (5.10). In that case, the signal precision is only limited by the shot and projection noise contribution to the signal.

This is the ideal case, however in the experimental reality we will always have some back-action remaining, depending on the duty cycle D. Due to the finite width of a measurement pulse and timing precision, we are able to reduce the back action, but not to completely remove it.

Figure 5.5 visualizes how the projection noise increases with increasing duty cycle width, assuming that the overlap between the recorded atomic cosine component $\hat{J}'_y$ and the signal are matched. The time traces for figure 5.5(a) were recorded while the pump and repump light were turned off with a 90 µs,

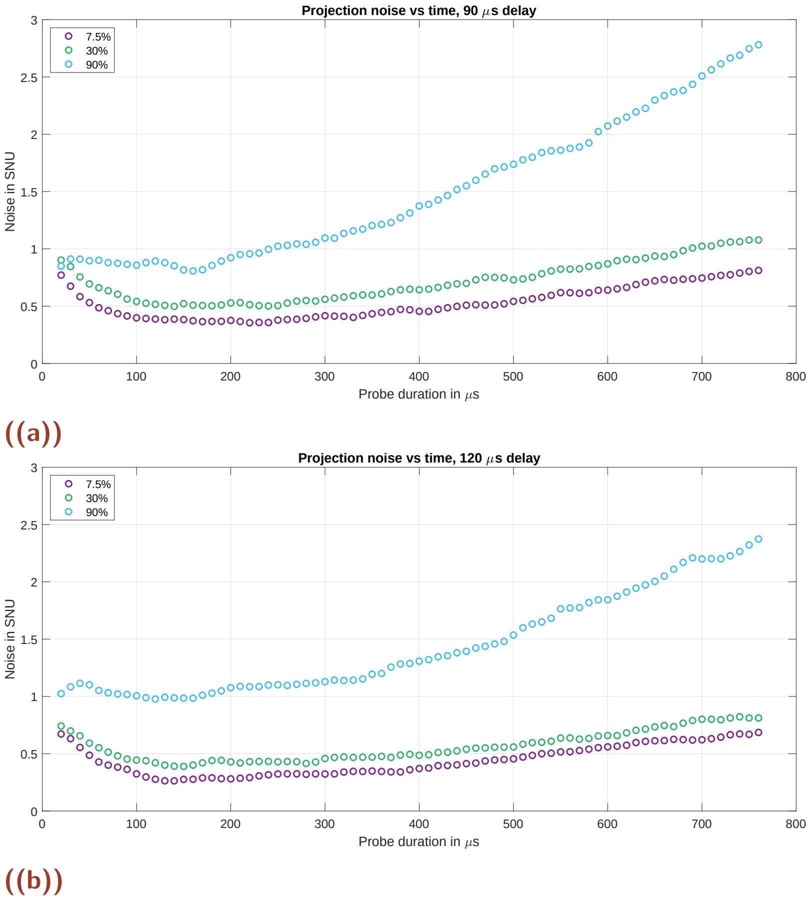

Figure 5.5: Increasing projection noise calculated from the corresponding recorded thermal noise with increasing probing time, shown for 7.5%, 30% and 90% probing duty cycle to visualize the influence of duty cycle on projection noise. for a) 90 µs delay and b) 120 µs delay between repump and pump turn off.

while the data for figure 5.5(b) was detected with a 120 µs delay between repump and pump turnoff as introduced in section 3.3. Both plots exhibit a similar evolution of the projection noise for related duty cycles in the respective plots. However, we see an overall reduced projection noise for an induced pump to repump delay of 120 µs, which supports the hypothesis established in section 3.3 that an increased atomic polarization due to a delay between the pump and repump turn off is beneficial to the system.

Summarizing the results above, we can see that the quality of the implemented QND measurement of the cosine component of $\hat{J}_y$ depends on the precise modulation of the probe pulses paired with the width of the probe light duty cycle. This Thesis covers the ideas and outcome of a stroboscopic QND measurement, further reading on the modulation functions can be found in [25].

5.3 Setup and Sequence

To apply a back-action reduction measurement, we probe stroboscopically, where the probing frequency is adjusted to match the spin precession of the doubled Larmor frequency. The following section will give an insight into the implementation of such a QND-type measurement to the experimental setup, pictured in figure 2.1. The corresponding trigger lines can be seen in figure 3.2. The probe beam waist has been adjusted so that we to vary the probe beam duty cycle in accordance with chapter 4, where a detailed explanation of the probe beam shaping can be found.
By using pMORS, introduced in chapter 3, the atomic polarization, transverse coherence time T_2 and the magnetic field quality have been confirmed to be experimentally sufficient. Compared to the resolved pMORS measurement, where we were operating with Larmor frequencies $\nu_L \approx 1.420\,\mathrm{MHz}$, we now reduce the Larmor frequency to $\nu_L \approx 720\,\mathrm{MHz}$ by approximately halving the bias magnetic field strength for stroboscopic probing.

Before we probe, we have to match the probing frequency with the Larmor precession as discussed in the previous section. To do so we set the approximated probing frequency with another function generator that sends a signal to the AOM setup for temporal beam shaping similar to the setup described in section 3.3. The recorded probing signal $\hat{S}_y^c$ is demodulated using a *lock-in amplifier* (LIA). When we record the signal for frequency and phase matching, we observe the resulting atomic spectrum by using a PicoScope with an interface provided by J. Mathiasen.

When the probe frequency is matched to overlap the Larmor precession by adjusting the frequency on the function generator, we observe a spectrum that exhibits a narrowed, single atomic signal centered around the Larmor frequency.
We then divide the obtained probing frequency by two and set the resulting frequency as the LIA reference signal frequency for demodulation.
Finally, by using an oscilloscope, we adjust the probing phase by overlapping the probing pulses with the maximum of the reference signal for the Lock-in amplifier as sketched in figure 5.3.
This has to be done whenever the Larmor frequency is changed.

We ensure that the cosine detection quadrature and the stroboscopic probe pulse overlap by maximizing Var$(\hat{S}_y^c)$, while Var$(\hat{S}_y^s)$ is minimized. That way we obtain an ideal phase between the shot noise components and ensure that the cosine detection quadrature and the stroboscopic probe pulse overlap.
To do so we record shot noise traces for both components at varying relative phases. This is the only measurement in the presented Thesis where both sine and cosine components of the signal $\hat{S}_y$ were recorded. The obtained data can be seen in figure 5.6, where we recorded shot noise traces for varying relative phases between the variation of the shot noise for the sine and cosine components.
For $(-32.5 \pm 0.2)^\circ$ phase difference between Var$(SN(\hat{S}_y^c))$ and Var$(SN(\hat{S}_y^s))$ we obtain maximally separated shot noise variances.

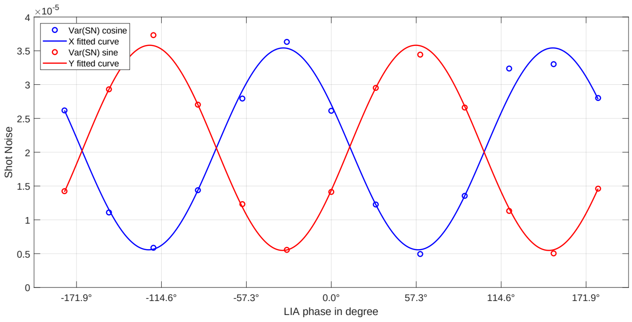

Figure 5.6: Sine and cosine component of the variation of shot noise for varying relative phases to determine the maximal phase difference

This is an initial optimization performed once in a while before setting up the spin squeezing measurements. Afterwards the Larmor frequency and probing phase are adjusted as described above.

5.4 Conditional Measurements

When we employ the stroboscopic back-action evasion protocol described in sections 5.2 and 5.3, we can split the obtained signal time traces into two regimes τ_A and τ_B. Both trace sequences are obtained by the same measurement, so they are correlated and can be used to study reduced conditional noise. During the analysis, we take information on the signal noise that was obtained during measurement time τ_A, and use it to condition the data recorded during a second time τ_B onto it. The measurement sequence can be seen in figure 5.8, where the data is measured in the same manner as in figure 5.4 and subsequently split into measurement times τ_A and τ_B in the analysis.

The following section will give an introduction to the idea and implementation of a conditional measurement. For in-depth calculations, chapter 14 in [21] is recommended and was used as my main source for this chapter.

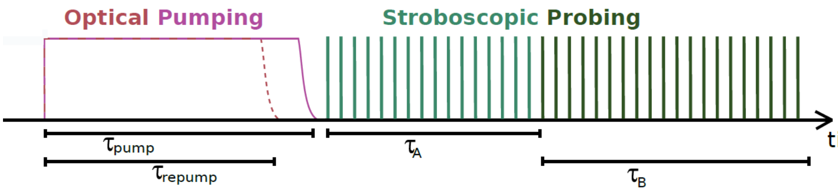

Figure 5.7: Sketched sequence for conditional stroboscopic probing. Stroboscopic optical pulses at twice the Larmor frequency, after the optical pumping has been turned off, stroboscopic optical pulses at twice the Larmor frequency, in the analysis the probing sequence is divided into a squeezing preparation with time τ_A and the squeezing verification time τ_B

As we have seen in section 5.2, the recorded signal is obtained by the output light field described by the Stokes operator $\hat{S}_y^c(t)$. When we record $\hat{S}_y^c(t)$ as the cosine component of the Lock-in amplifier (LIA), we refer to the obtained signal as $\hat{X}$. For the conditional measurement we split that signal into $\hat{X}_A$ for times $\tau_A \in [0, t_A]$ and $\hat{X}_B$ for times $\tau_B \in [t_A, t_A + t_B]$. Both times τ_A and τ_B are smaller than the transverse coherence time T_2.

To introduce conditional analysis, we first look into each of the sequences individually. For each of the signals $i \in [A, B]$, the signal noise

$$\mathrm{Var}(\hat{x}_i) = \frac{\mathrm{Var}(\hat{X}_i) - EN_i}{SN_i} - 1, \tag{5.12}$$

where $\hat{x}_i$ is the signal $\hat{X}_i$ that is first corrected by the electronic noise and subsequently normalized to shot noise units (SNU) of the corresponding signal.

From here we can condition signal noise $\mathrm{Var}(\hat{X}_A)$ onto $\mathrm{Var}(\hat{X}_B$ by minimizing the the conditional variance with $\frac{\mathrm{Cov}^2(\hat{X}_B, \hat{X}_A)}{\mathrm{Var}(\hat{X}_A)}$ [25].

When we now condition signal $\hat{X}_B$ onto $\hat{X}_A$, we see that

$$\mathrm{Var}(\hat{x}_{B|A}) = \frac{\mathrm{Var}(\hat{X}_B)}{SN_B} - \frac{\mathrm{Cov}^2(\hat{X}_B, \hat{X}_A)}{SN_B \cdot \mathrm{Var}(\hat{X}_A)} - 1 = \frac{\mathrm{Var}(\hat{X}_B)}{SN_B} - \alpha. \tag{5.13}$$

For $\alpha > 0$ we observe a reduction of the conditional signal noise $\mathrm{Var}(\hat{X}_{B|A})$ by α compared to the unconditional noise obtained during time τ_B. The conditional signal noise is dependent on the length of both the measurements τ_A and τ_B and on the noise contributions $\mathrm{Var}(\hat{X}_A)$ and $\mathrm{Var}(\hat{X}_B)$ and hence on the duty cycle D as discussed in section 5.2.

The influence of the conditional measurement can be seen in figure 5.8, where each measurement was taken with a 15 % duty cycle and varying delay times between the repump and pump light turnoff. All three plots have in common that we see a significant reduction of the conditional noise $\hat{X}_{B|A}$ compared to the unconditional noise $\hat{X}_B$. The overall noise reduction of 77 ± 6 % is the same for all three plots. For figure 5.8(a), where both pumping beams were turned off simultaneously, $\hat{X}_B$ is increasing faster than for the other two plots and as a result the conditional noise is larger here than for both other plots in figure 5.8(b) and 5.8(c).

The noise contribution for both conditional and unconditional measurement in figure 5.8(b) and 5.8(c), where we introduce a delay between the pump and repump turnoff off 70 µs and 120 µs resemble each other. Here the unconditional noise is not increasing as fast as without a repump to pump turnoff delay, supporting the hypothesis that an introduced delay might be beneficial for the performance of the physical system.

To summarize this chapter so far: We studied various sources of noise that compromise the atomic signal, including quantum back-action noise. We further introduced a stroboscopic QND measurement to reduce the back-action and showed that a conditional measurement can suppress the signal noise compared to an unconditioned measurement. By combining these efforts, we can record conditional spin squeezing on the recorded signal. The total level of spin squeezing is determined by the squeezing parameter

$$\zeta^2 = \frac{\mathrm{Var}(\hat{X}_{B|A}) - SN_B - EN_B}{\mathrm{Var}(\hat{X}_B) - SN_B - EN_B}, \tag{5.14}$$

the ratio between the conditional and unconditional noise on the signal for the second probing time τ_B. We verify the degree of spin squeezing with the recorded data traces on the dB scale and see that the signal-to-noise ratio has

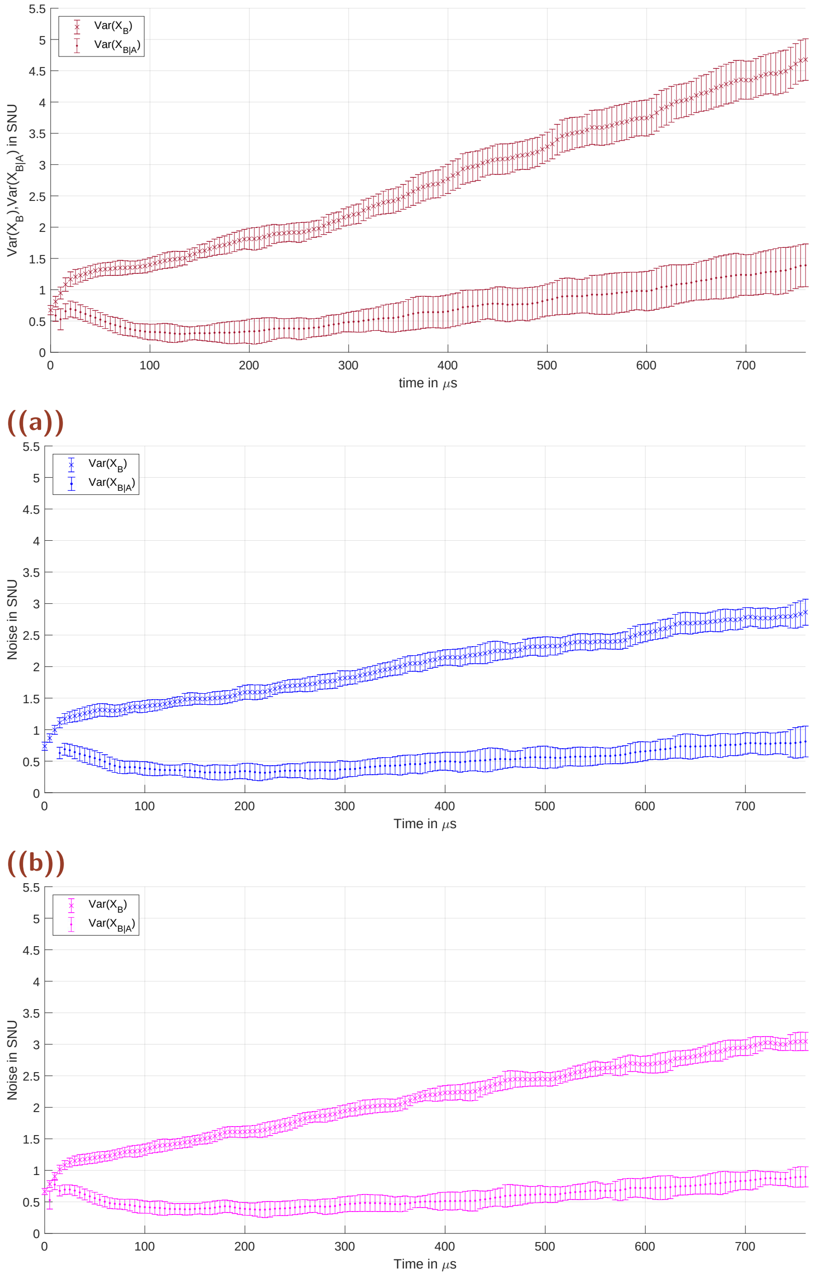

((a))

((b))

((c))

Figure 5.8: Comparison of the unconditional noise with conditional noise, both obtained during time τ_B for duty cycle $D = 15\,\%$ for a) zero delay, b) 70 µs delay, c) 120 µs delay between pump and repump turnoff, where repump was turned off first

reduced to

$$SNR^{SQ} \propto \frac{\tilde{\kappa}}{\sqrt{(1+\zeta^2 \frac{\tilde{\kappa}^2}{2})}}, \tag{5.15}$$

compared to equation (5.8) for a continuous measurement and compared to equation (5.10) for a back-action reduced measurement.

As we see in equation (5.15), with a successful conditional squeezing measurement we can suppress the back-action term in equation (5.8) ($\propto \kappa^4$) and further reduce the projection noise ($\propto \kappa^2$) by a factor ζ^2.

The influence of the different duty cycles and additional spin squeezing can be seen in figure 5.9.

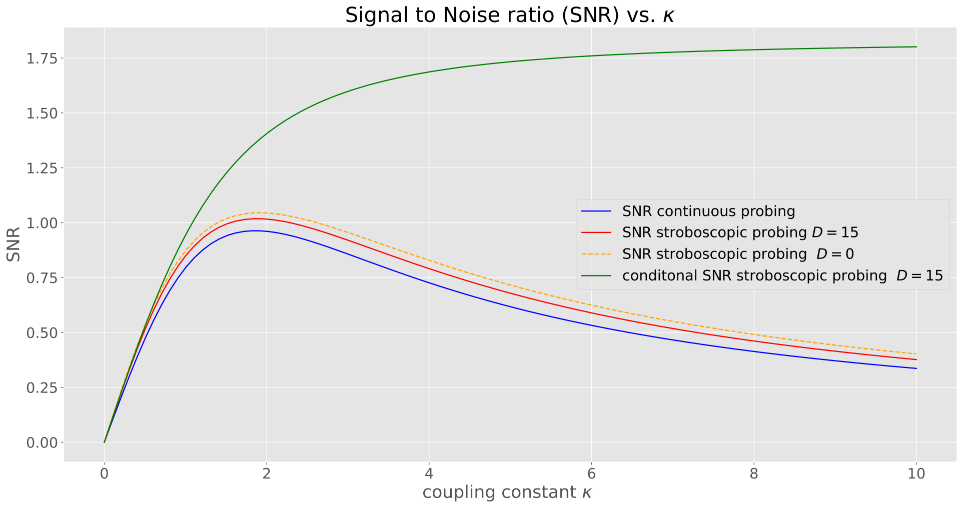

Figure 5.9: Qualitative comparison of SNR for continuous measurement as seen in eq. (5.8), stroboscopic measurement as seen in eq. for the $D = 15\%$ and for a δ-peak like probing pulse with $D = 0\%$ in eq. (5.10) and SNR for conditional spin squeezing for $D = 15\%$ and $\zeta = 0.6$, which equals -4.44 dB squeezing.

[25] has shown that we can rewrite the squeezing parameter in equation (5.14) to

$$\zeta^2 = \frac{1}{1+\tilde{\kappa}^2} + \eta_\tau, \tag{5.16}$$

where η_τ is an additional term accounting for the increase of uncertainty due to decoherence effects. η_τ is proportional to the number of decoherence events during the measurement time τ. The QND interaction strength $\tilde{\kappa}$ is related by $\tilde{\kappa}^2 \propto \eta_\tau d_0$ to the decoherence η_τ and the optical depth d_0. '

To obtain a high degree of squeezing, we consequently require a large optical depth. However, by introducing a delay between pump and repump we decrease the optical depth, indicating that despite having a higher polarization, we might have to sacrifice squeezing for introduced delays that extend a threshold of optical depth.

5.5 Conditional Spin Squeezing Measurement

For a previous publication of the presented setup [27], the spin squeezing measurement was performed with a minimal probe beam duty cycle $D = 15\,\%$, which was limited by the attainable stroboscopic probing pulses of the experimental setup. By updating the setup to allow for lower duty cycles and recording signal traces with $D < 15\,\%$, we hope to reduce back-action noise of the signal further than previously observed as discussed in section 5.2.
With the updated setup it is possible to obtain a duty cycle of $7.5\,\%$ with a probing frequency $\nu_{\text{probe}} \approx 1.42\,\text{MHz}$. It should be noted that when we change the duty cycle, the probe power has to be adjusted so that the atomic ensemble interacts with the same number of photons for every measurement cycle.
We further introduced a delay between the turnoff of the pump to repump light. That way we are able to increase the atomic polarization, as we have seen in section 3.3. In figure 5.8 we could confirm that an induced delay of both $70\,\mu\text{s}$ and $120\,\mu\text{s}$ did indeed reduce the projection noise level.
When we refer to 'delay' in the following section, we refer to the time the repump light was turned off earlier than the pump light.

For all the measurements presented in this section, the cell was not taken out of the shield and the magnetic bias field and probing frequency were only slightly adjusted from measurement to measurement. Each plot presented here was measured with 12 data sets, containing 4000 measurement sequence repetitions.

Figure 5.10 presents time traces that were stroboscopically recorded and subsequently analyzed to exploit conditional spin squeezing. The data is shown for several duty cycles with varying repump to pump delay times and analyzed for the first measurement time τ_A. We set $\tau_B = 40\,\mu\text{s}$ for all three subplots. The amount of spin squeezing is the reduction of the signal noise

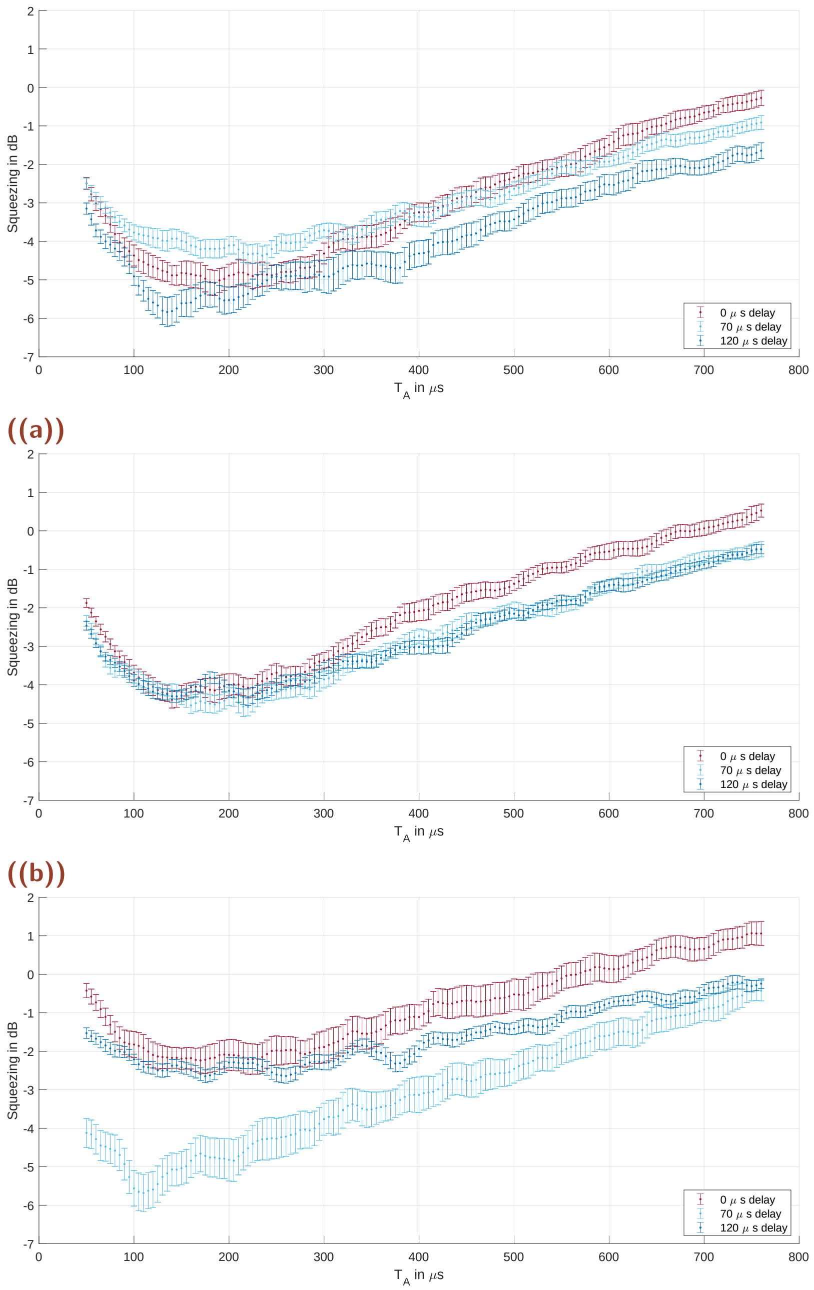

((a))

((b))

((c))

Figure 5.10: Comparison of the conditional spin squeezing results for a duty cycle a) $D = 7.5\,\%$, b) $D = 15\,\%$ and c) $D = 30\,\%$, where for each duty cycle a graph with 0 µs (red), 70 µs (light blue) and 120 µs (dark blue) delay between the repump and pump light turn off is presented. The error bars are obtained by accounting for 12 data traces, each recorded with 4000 averages. τ_B set to 40 µs

compared to the photon shot noise of the measurement in decibel dB.
Figure 5.10(a) shows spin state squeezing results for a duty cycle $D = 7.5\,\%$. Without any delay between the pump and repump turnoff, we observe the best squeezing results for of all three duty cycles pictured here, confirming that a reduced duty cycle does indeed improve the measurement results. By halving the duty cycle, we were able to reduce the spin squeezing results by approximately 1 dB compared to the previously best result, published in [27] for $D = 15\,\%$.
Nevertheless we observe increased fluctuations and longer error bars with this duty cycle compared to the presented larger duty cycles. This effect can be especially seen for traces that were recorded with non-zero delay times.
As we have seen in equation (5.16), the squeezing parameter ζ is dependent on the optical depth of the ensemble. When we now introduce a delay, which effectively decreases the optical depth, while probing with such a short duty cycle, we are not able to observe atom-light interaction with sufficient strength to observe improved squeezing results compared to results obtained with $D = 15\,\%$.

In figure 5.10(b), we see the spin state squeezing evolution during probing time τ_A for a probing light duty cycle $D = 15\,\%$. The obtained squeezing results for zero delay are improved compared to the squeezing results published in [27]. This both reassures that we successfully recovered and improve the experimental setup.
However, we observe that squeezing for zero delay degrades faster in the presented work than in [27]. This could be due to a change the magnetic fields settings or due to a degradation of the cell and its spin-preserving coating. Since the squeezing for delay times of 70 µs and 120 µs degrade slower than for zero delay, it could have also been that this specific measurement was disturbed by traffic in the lab.

Figure 5.10(c) visualized how an increased duty cycle influences the outcome of the squeezing analysis. Here the presented data was recorded with a duty cycle $D = 30\,\%$. The maximally attainable squeezing has reduced by half compared to squeezing with $D = 15\,\%$.
The measurement for 70 µs shows large fluctuations and increased error bars, which is an indication that the measurement is error-prone. This plot was included to present an unreliable result, which might have been recorded while one of the lasers unlocked or happened due to other disturbances in

the lab. It does not show reliable data but should rather represent a faulty plot.

From figure 5.10 we were able to obtain squeezing for all three duty cycles with all three delay settings for up to 500 µs.
Additionally, we can see that a delay between the pump and repump turnoff is indeed beneficial to the maximal squeezing outcome. Independent of the duty cycle, for every figure in 5.10, the squeezing results were improved by the delay, with the only exception being the 70 µs delay recorded with $D = 7.5\,\%$.

We obtain an optimal setting for τ_A from figure 5.10, where independently of the duty cycle or delay, the best results for squeezing were obtained for measurement times $\tau_A \in [170, 210]$µs. Moving on we will set $\tau_A = 190$ µs to investigate τ_B.

Figure 5.11 presents the evolution of the spin squeezing results obtained for the same duty cycles $D = 7.5\,\%$ and $D = 15\,\%$ as present in figure 5.10(a) and 5.10(b), which were analyzed with a fixed value $\tau_B = 40$ µs.
In figure 5.11(a), we see spin squeezing results obtained by stroboscopic probing with a duty cycle 7.5 %. For zero and 70 µs delay time we observe that the spin squeezing can be maintained by 50 % during probing time $\tau_B = 150$ µs. The data for 120 µs delay has reduced by 50 % after $\tau_B = 80$ µs. However in that case, the curvature for earlier times of the squeezing evolution is steeper and exhibits larger error bars than the other two plots, indicating that either the measurement or the conditional analysis are limited in precision.
In comparison, we see the evolution of the spin squeezing results for a duty cycle = 15 % over time τ_B. For an induced repump to pump delay we observe that the spin squeezing has reduced by 50 % after 150 µs probing time, where the zero delay plot has degraded after 130 µs.

Summarizing figures 5.10 and 5.11, we see that an introduced delay between the turnoff of the repump and pump light has a positive influence on the spin squeezing results, especially for a probing sequence with $D = 15\,\%$. For a duty cycle $D = 7.5\,\%$ the effect is reproducible. However due to the limited probing time with the reduced duty cycle, the sequence is more likely to be affected by time jitters or mismatched frequencies.

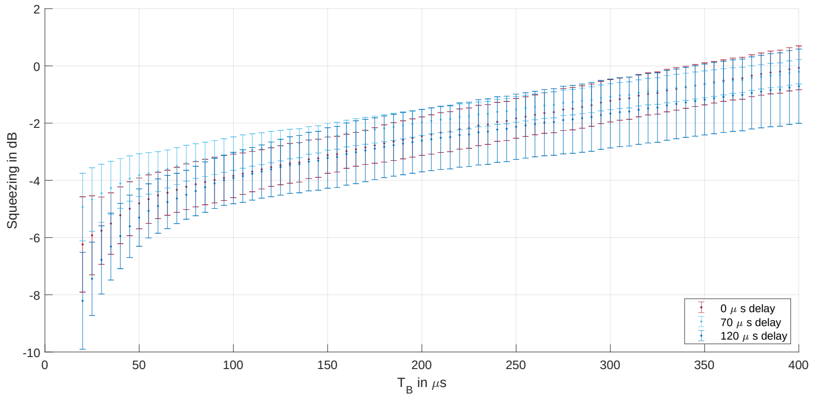

((a))

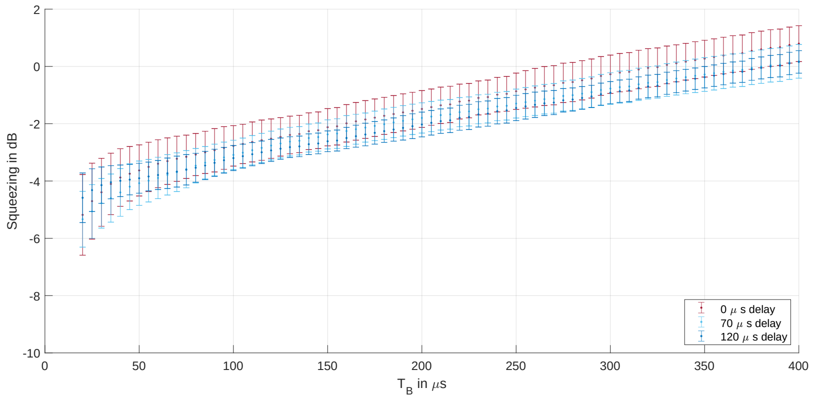

((b))

Figure 5.11: Comparison of the conditional spin squeezing results for a duty cycle a) $D = 7.5\,\%$ and b) $D = 15\,\%$, where for each duty cycle a graph with $0\,\mu\text{s}$ (red) and $70\,\mu\text{s}$ (light blue) delay between the repump and pump light turn off is presented. The error bars are obtained by accounting 12 data traces, each recorded with 4000 averages. τ_A set to $190\,\mu\text{s}$

6

Towards Detection of a Conductive Object

In the previous chapters we presented atom-light interaction centered around the heart of the experiment, the Cesium vapor cell.
We have seen in the previous sections that the collective spin orientation of the atomic ensemble exhibits a high sensitivity towards changes in the magnetic field. We can exploit that feature to detect magnetic fields or flowing current and utilize the experimental setup as an atomic magnetometer through magneto-induction tomography (MIT) as proven in [13], [21], [27].
Ultimately the goal of this setup will be to detect the presence of a conductive sample. At the time of writing this Thesis, these measurements were in preparation, so here we present the optimization of the preparing measurements.

The working principle of MIT has been known and applied in many different forms over the last decades [17], with the underlying principle following a similar idea. A conductive sample is placed between two electromagnetic coils. One of the coils is driven by an RF current to generate an oscillating magnetic field. That field acts on the conductive sample and induces eddy currents. In return, the field generated by the eddy currents is picked up by an anti-parallel second coil, the pick-up coil. By recovering the information obtained through the secondary coil, we can deduct information about the sample.

We can translate the MIT principle to the related experimental setup.
Again we are working with the experimental setup in figure 2.1, described in chapter 2. Similar to the introduction above, we send an RF field. That field is oriented in z-direction, transverse to the magnetic bias field in x-direction and is driven by a number of RF cycles. The RF coils generating the field are in an anti-parallel (anti-Helmholtz) setting so that in the absence of a conductive object, the RF field does not disturb the optically pumped spin ensemble. In that case the spin ensemble possesses zero transverse mean spin.

However, if we add a conductive object between the RF coils and the cell, the RF field induces eddy currents in the sample. Those eddy currents disturb the balanced magnetic field so that the spin orientation of the atomic ensemble changes. This creates a mean transverse spin component that we can optically read out by sending a probe beam in a homodyne detection scheme. By probing the transverse mean spin, we can conclude information about the sample, e.g. its position relative to the ensemble

As we have seen in chapter 5, we are able to reduce the signal noise of the recorded probe signal. Different from a classical MIT setup, we are able to suppress quantum back-action noise and reduce the noise contribution trough conditional spin squeezing measurement.
When we apply this principle and use the atomic ensemble as pick-up coil, we are able to obtain a quantum-enhanced sensing protocol with increased sensitivity [21], [27].

To apply the conditional measurement describe in section 5.15, we again resort to a conditional measurement. The probing time is split between the squeezing preparation time τ_A and squeezing verification time τ_B. Different to earlier, we now introduce a gap with time τ_{gap} in which we send an RF field. The whole sequence can be seen in figure 6.1.

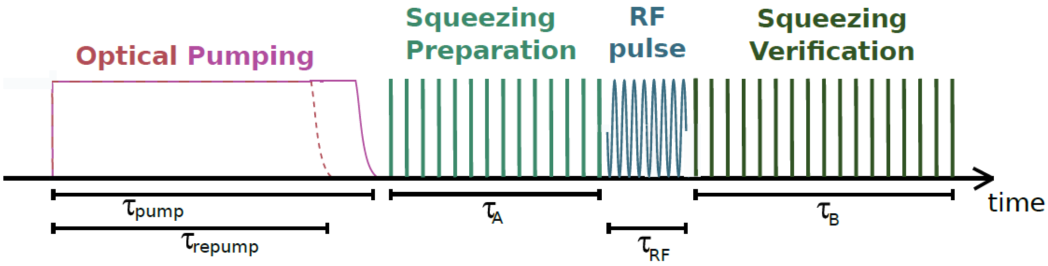

Figure 6.1: Sketched sequence for conditional stroboscopic probing. Stroboscopic optical pulses at twice the Larmor frequency. After the optical pumping has been turned off, stroboscopic optical pulses at twice the Larmor frequency are sent during time τ_A, then an RF pulse with a fixed number of cycles is sent during τ_{gap} and finally we probe again in the squeezing verification time τ_B

In chapter 5.5 we determined an optimal squeezing preparation time $\tau_A = 190\,\mu\text{s}$. That value holds for duty cycle $D = 15\,\%$ and $D = 7.5\,\%$ for both $0\,\mu\text{s}$ and $70\,\mu\text{s}$ repump to pump turnoff times.
We have further seen that the squeezing degrades with increasing time τ_{gap},

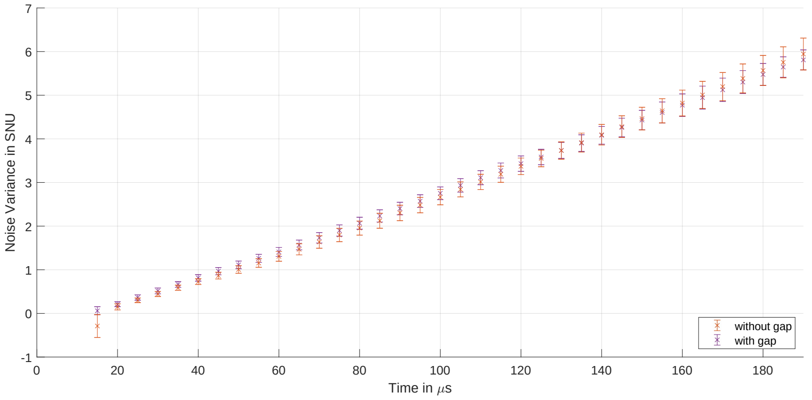

Figure 6.2: Comparison of the signal variance $\mathrm{Var}(\hat{X}_A)$ recorded during time $\tau_A \in [0, 190]$ µs with 15 % duty cycle and zero pumping delay with $\tau_{\mathrm{gap}} = 0$ µs (orange), as seen in figure 5.10 and $\tau_{\mathrm{gap}} = 50$ µs (purple)

so the longer τ_{gap}, the less squeezing we can be obtained.

Firstly we start by repeating the squeezing measurements as seen in section 5.5 with an introduced gap between τ_A and τ_B. This helps to determine the gap length τ_{gap}, while maintaining squeezing results.
Since τ_A is independent of τ_{gap} or τ_B, we expect the recorded signal variance $\mathrm{Var}(\hat{X}_A)$ to be similar to measurements presented in section 5.5. A comparison of both signal variances during time τ_A with and without an introduced gap between τ_A and τ_B can be seen in figure 6.2. Here we see that both signal noises indeed overlap. It should be noted that both measurements were obtained with the same number of averages and repetitions.

We want to find a gap length that is long enough to fit sufficient RF cycles, while keeping it short enough to maintain spin squeezing results.
The results for various gap and delay times and their influence on the spin squeezing results can be seen in figure 6.3. The data was recorded was repeated 8 times with 4000 averages. The presented data was recorded with a spin preparation time $\tau_A = 190$ µs and an introduced gap of $\tau_{\mathrm{gap50,0}} = 50.2$ µs and $\tau_{\mathrm{gap50,70}} = 50.47$ µs for zero and 70 µs delay times depicted in red and blue in figure 6.3(a) respectively. In comparison the larger gap in figure 6.3(b) was recorded with $\tau_{\mathrm{gap100,0}} = 100.38$ µs (red) and $\tau_{\mathrm{gap100,70}} = 100.21$ µs (blue). The increased gap is set so that the reference signal and the probing pulse phase overlap. Depending on the phase of the probing pulse to the LIA reference, we add a time in the ns scale to account for the phase difference.
We observe increased error bars compared to the squeezing results seen in figure 5.11. Nonetheless we can observe mean values that reassure squeezing

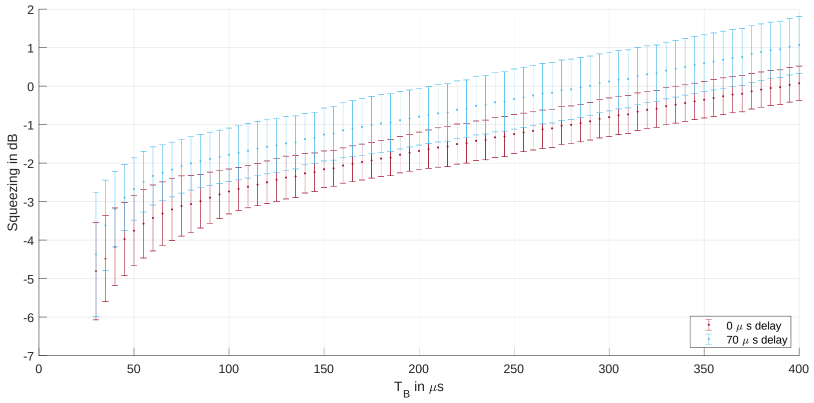

((a))

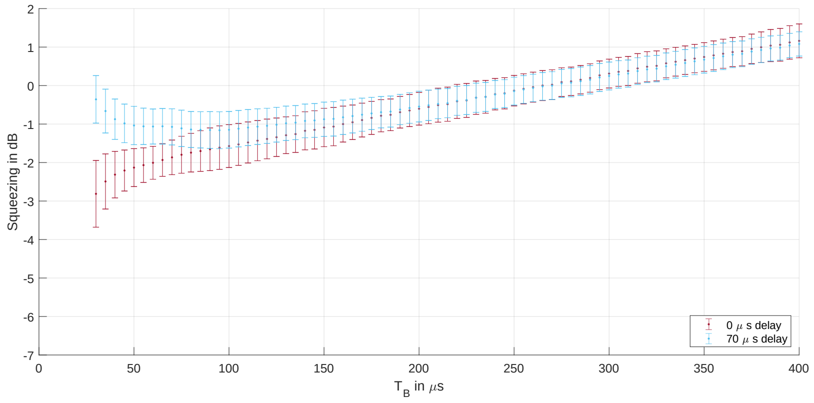

((b))

Figure 6.3: Comparison of the conditional spin squeezing results for a duty cycle $D = 15\,\%$ with an introduced gap between $\tau_A = 190\,\mu s$ and τ_B for a) $\tau_{\text{gap}} = 50\,\mu s$ and $\tau_{\text{gap}} = 100\,\mu s$. For each gap length a graph with $0\,\mu s$ (red) and $70\,\mu s$ (light blue) delay between the repump and pump light turn-off is presented. The error bars are obtained by accounting 8 data traces, each recorded with 4000 averages.

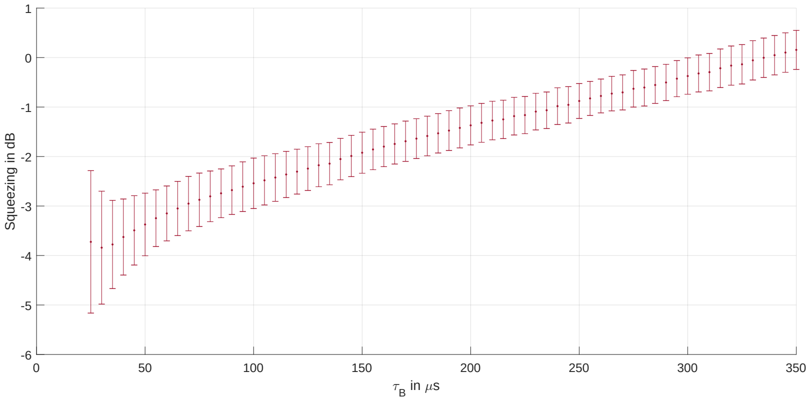

Figure 6.4: Evolution of spin noise squeezing with increasing squeezing confirmation time τ_B for $\tau_A = 190\,\mu s$, $\tau_{gap} = 50.27\,\mu s$ with 34 RF cycles. Data recorded with 4000 averages with 9 repetitions

results obtained in the last chapter. Due to an increased temporal separation between the end of τ_A and the beginning of τ_B, the squeezing results for $\tau_{gap} = 100\,\mu s$ are lower than for $\tau_{gap} = 50\,\mu s$.

Moving forward we will hence introduce an RF pulse with a length of $\tau_{gap} = 50\,\mu s$, during which we are able to send 34 RF cycles to the RF coils to induce eddy currents. The RF amplitude is set to 100 mA.
Exemplary evolution of spin noise squeezing with increasing squeezing confirmation time τ_B can be seen in figure 6.4. Here we introduced a gap $\tau_{gap} = 50.27\,\mu s$ and sent 34 RF cycles. The squeezing preparation time $\tau_A = 190\,\mu s$ was set and the data traces were obtained with 4000 averages at 9 repetitions. We observe that the spin squeezing has degraded by 50 % 75 µs after it reached its lowest value.

After introducing a gap with an RF field, we are finally ready to move on to detect a conductive sample!

Discussion

7

7.1 Conclusion and Outlook

In this Thesis, we presented an overview on the improvements of a previously used atomic ensemble of pumped Cesium atoms for atom-light interaction for a quantum-enhanced sensing protocol.

The first chapter introduced the underlying physics of the individual components of the experimental setup. Here the main focus was set on an introduction to atomic physics based on the example of the Cesium ensemble used in this Thesis.

With this first understanding of the underlying physics, we moved on to describe pulsed MORS in chapter 3, a technique used to quantify the quality of the physical setup. Following a proposal in [21], we implemented a delay between the repump to pump light turnoff to increase the atomic polarization, as well as implemented a complex fitting routine. Using pMORS we could indeed confirm an improvement of the atomic polarization of (3.8 ± 1.1) % by implementing a delay time between 70 µs and 140 µs compared to a simultaneous turnoff. A further extension of the delay would not improve the polarization, but decrease the optical depth.

For the previous publication [27], the width of the duty cycle presented a limitation to the stroboscopic probing scheme for back-action noise reduction. To improve this setup, we investigated the probe beam modulation and the temporal shaping of the probe beam duty cycle. With an updated probe beam path in front of the modulating AOM, we were able to reduce the minimum duty cycle from previously 15 % to 7.5 % for a probing frequency of $\nu \approx 1.42\,\mathrm{MHz}$.

With the implemented delay and updated possibility to reduce the duty cycle, we then moved on to perform conditional spin squeezing measurements to test the implemented experimental changes.

We were able to reproduce previous squeezing results and confirm a successful noise reduction as seen in [27]. Further, we could confirm that an

induced delay between 70 and 120 µs improves the polarization of the atomic ensemble to an extent that helped to reduce conditional noise further.
Further, we were able to perform stroboscopic probing with a minimal duty cycle of 7.5 %. Here we observed a reduction of the back-action noise compared to measurements with larger duty cycles. However, with a reduced probing time per sequence cycle, we increased the likeliness of time-sensitive errors so that the gain of the attainable squeezing was lower than expected.
With the results obtained for the conditional squeezing measurements, we were able to determine an optimal squeezing preparation time $\tau_A = 190\,\mu\text{s}$. Knowing τ_A, we could implement a gap between the squeezing preparation time τ_A and a squeezing confirmation time τ_B of $\tau_{\text{gap}} = 50\,\mu\text{s}$ to introduce 34 RF cycles.

So what is next?

The immediate next step with the relating stroboscopic probing scheme will to test for conductive objects. Those tests were in preparation at the time of writing this thesis.

The experimental setup is constructed to perform a quantum-enhanced sensing protocol to improve magneto induction tomography (MIT) by exploiting quantum mechanical effects.
Compared to the classical counterpart [13], we are able to eliminate measurement-induced back-action and employ a conditional measurement scheme. By implementing these features, we hope to decrease the noise contribution compromising the signal and to ultimately increase the measurement sensitivity compared to classical MIT protocols. Since the center of the experimental setup lies within the atoms in the cell, all experimental results are dependent on the quality of the cell. As we have seen an increased frequency at which we have to remove the cell from the shield to recure it, exploring other cell types might be beneficial to improve a higher experimental consistency and a longer spin coherence time. However by changing to a cell with different dimensions, the magnetic bias field would need to be updated to remain homogeneously.

When we employ pMORS in this thesis we use it to determine the polarization and the spectral linewidth of the pumped atomic spin state. As we have seen, we can improve the polarization of the cell by introducing a delay between the repump and pump turnoff.

The spin coherence time is influenced by the magnetic field homogeneity. By improving the magnetic field homogeneity further, we can potentially improve the bias field homogeneity and reduce decoherence effects to extend the spin coherence time.

7.2 Acknowledgements

As concluding words, I would like to start by thanking Professor Eugene Polzik for giving me the opportunity to join the research group at QUANTOP for both a research project and my Master's Thesis project. He sparked the joy of Quantum Optics during his lectures that kept my curiosity ever since. I deeply appreciate the chance to participate in the scientific work in the cell lab.

A huge thank you to Rebecca Schmieg for her attention and patience to answer my questions to help me understand the tasks at hand and who trained me in the lab. Even at busy times, she always found time to highlight the progress, provide helpful insights and to share her thoughts. She also provided very helpful comments when writing this Thesis. I am very thankful that I got to work together with her.

I would like to thank everyone at QUANTOP for creating such a welcoming and curious work environment. A heartfelt thank you to the fellow Master students Alkis and Robin for their companionship.

On a more personally note, I would like to thank my husband David and my friends and family for always bearing with me and supporting me during the process of working on this Thesis. I am very thankfull. Especially Merlijn and Luna were great in giving words of reassurance and compassion.

Bibliography

[1] *Acousto-Optic Modulation*. AN 0510. Isomet Corporation. 2010.

[2] *Acousto-Optical Theory Application Notes*. Theory 2013. AA Opto Electronic. 2013.

[3] Marcis Auzinsh, Dmitry Budker, and Simon Rochester. *Optically polarized atoms: understanding light-atom interactions*. Oxford University Press, 2010.

[4] Christian Folkersen Baerentsen. „Generation of non-classical states in a hybrid spin-optomechanical system“. PhD thesis. University of Copenhagen, Niels Bohr Institute, June 2020.

[5] Benjamin Bederson. *More things in heaven and earth: a celebration of physics at the millennium*. Springer Science & Business Media, 2012.

[6] J. C. van den Bosch. *The Zeeman Effect*. Springer Berlin Heidelberg, 1957.

[7] Brian Harold Bransden and Charles Jean Joachain. *Physics of atoms and molecules*. Pearson Education India, 2003.

[8] Christopher J Foot. „Atomic physics; Atomphysik“. In: (2011).

[9] Christopher Gerry and Peter L Knight. *Introductory quantum optics*. Cambridge university press, 2005.

[10] Klemens Hammerer, Anders S Sørensen, and Eugene S Polzik. „Quantum interface between light and atomic ensembles“. In: *Reviews of Modern Physics* 82.2 (2010), p. 1041.

[11] T Holstein and Hl Primakoff. „Field dependence of the intrinsic domain magnetization of a ferromagnet“. In: *Physical Review* 58.12 (1940), p. 1098.

[12] Kurt Jacobs. *Quantum measurement theory and its applications*. Cambridge University Press, 2014.

[13] Kasper Jensen *et al.* „Detection of low-conductivity objects using eddy current measurements with an optical magnetometer“. In: *Physical Review Research* 1.3 (2019), p. 033087.

[14] Brian Julsgaard. „Entanglement and Quantum Interactions with Macroscopic Gas Samples“. PhD thesis. University of Copenhagen, Niels Bohr Institute, Oct. 2003.

[15] Walter Koechner. *Solid-state laser engineering*. Vol. 1. Springer, 2013.

[16] Hanna Krauter. „Generation and application of entanglement of room temperature ensembles of atoms“. PhD thesis. University of Copenhagen, Niels Bohr Institute, Jan. 2011.

[17] MS Badri Mansor *et al.* „Magnetic induction tomography: A brief review“. In: *J. Teknol* 73.3 (2015), pp. 91–95.

[18] Daniel J McCarron. „A Guide to Acousto-Optic Modulators“. In: 2007.

[19] Katsuaki Sato and Takayuki Ishibashi. „Fundamentals of Magneto-Optical Spectroscopy“. In: *Frontiers in Physics* 10 (2022), p. 946515.

[20] Rudolf Schieder. „Bemerkungen zur Kohärenten Optik“. Publication. I. Physikalisches Institut Universität zu Köln.

[21] Rebecca Schmieg. „Collective Spin-Oscillators for Light-Atom Interfaces“. PhD thesis. University of Copenhagen, Niels Bohr Institute, Apr. 2023.

[22] Heng Shen. „Spin squeezing and entanglement with room temperature atoms for quantum sensing and communication“. PhD thesis. Niels Bohr Institute, University of Copenhagen, Dec. 2014.

[23] Hans Stærkind. „Magnetic bias-field coil design and characterization“. Project Report. University of Copenhagen, Niels Bohr Institute, 2015.

[24] Daniel A. Steck. „Characterizing the spin state of an atomic ensemble using the magneto-optical resonance method“. In: (1998).

[25] Georgios Vasilakis *et al.* „Generation of a squeezed state of an oscillator by stroboscopic back-action-evading measurement“. In: *Nature Physics* 11.5 (2015), pp. 389–392.

[26] Tatjana Wilk. *Quantum Interface between an Atom and a Photon*. Feb. 2008.

[27] Wenqiang Zheng *et al.* „Entanglement-enhanced magnetic induction tomography“. In: *Physical Review Letters* 130.20 (2023), p. 203602.